

Thermal Relaxation and Ground State Ordering in Artificial Spin Ice

Inauguraldissertation

zur Erlangung der Würde eines Doktors der Philosophie
vorgelegt der
Philosophisch-Naturwissenschaftlichen Fakultät
der
Universität Basel
von

Alan Farhan
aus Wien, Österreich

Basel, 2014

Genehmigt von der Philosophisch-Naturwissenschaftlichen Fakultät

auf Antrag von

Prof. Dr. Frithjof Nolting

Prof. Dr. Christoph Bruder

Basel, den 24.06.2014

Prof. Dr. Jörg Schibler
Dekan der Philosophisch-
Naturwissenschaftlichen Fakultät

Acknowledgments

Officially declared a “one man show” with this thesis, a PhD project is actually a result of successful teamwork, starting from careful introductions to the research topic up to thorough discussions and assistance in publishing the acquired data. Therefore, it is important to acknowledge the efforts some people invested into my work at PSI.

Rajesh Chopdekar, Elena Mengotti and Anja Weber, I always considered myself lucky to have you around me as mentors, during my first few months at PSI. A special thanks here belongs to Anja Weber for a very careful and critical introduction into clean room equipment and sample fabrication, in general. Being a stubborn and bad listener at times, your efforts can not be overestimated.

Being limited in my programming skills, I really appreciated the assistance I received from both my colleagues Luca Anghinolfi and Jonathan Perron, regarding that matter. Both their enthusiastic contributions accelerated many aspects of analyzing my beamtime data.

Ana Balan and Marcus Wyss, I can not imagine how my beamtimes would have ever worked without the fun and positive attitude you guys brought into your daily work.

A very special thanks belongs to Peter Derlet and Armin Kleibert for all their support and discussions. None of my publications would have been possible without your great contribution.

I also want to use the opportunity to thank my supervisor, Laura Heyderman, for giving me the opportunity to join her group and work on such an exciting project. I always appreciated her patience and ability to motivate me to develop my strengths and work on my weaknesses, which I think were many, upon my arrival to PSI.

Last but not least, special thanks also go to my doctor father from the University of Basel, Frithjof Nolting. Thank you for your support during my beamtimes and useful discussions at all stages of my PhD.

Abstract

We have studied the thermal relaxation of artificial spin ice in its two main geometries, namely artificial square ice and artificial kagome spin ice. Using synchrotron based photoemission electron microscopy we are able to directly observe how artificial square ice systems find their way from an energetically excited state to one of the two degenerate ground state configuration. On plotting vertex type populations as a function of time, we can characterize the relaxation, which occurs in two stages, namely a string and a domain regime. Kinetic Monte Carlo simulations agree well with the temporal evolution of the magnetic state when including disorder, and the experimental results can be explained by considering the effective interaction energy associated with the separation of pairs of vertex excitations.

While a simple thermal annealing procedure, that involved one cycle of heating and cooling the sample above and below the blocking temperature ($T_B = 320 - 330$ K), proved to be very effective in achieving long-range ordered ground state configurations in artificial square ice, the ability of achieving the same goal in artificial kagome spin ice is shown to become increasingly difficult with increasing system size. By first focusing on the so-called building block structures of artificial kagome spin ice, with system sizes ranging from a single ring up to seven-ring structures, we proved that the ability to access the ground state is lost at a system size comprising seven kagome rings. Extrapolating the result to extended arrays of artificial kagome spin ice, we conclude that a long-range ordered ground state is unlikely to be achieved in an infinite array of artificial kagome spin ice. This conclusion is later confirmed by investigating thermal annealing on extended arrays of artificial kagome spin ice.

Finally, we explored a potential optimization of thermal annealing on artificial kagome spin ice. For this purpose, we patterned artificial kagome spin ice arrays with lower blocking temperatures ($T_B = 160$ K), hoping that the blocking temperature to be below the predicted temperatures for phase transitions into ordered configurations. Both continuous and stepped cooling from temperatures around 370 K down to 140 K proved to be inefficient in achieving ground state configurations. We then applied an annealing procedure that involved repeated heating and cooling just slightly around the blocking point ($T_B = 160$ K), thus allowing the system slow attempts in accessing ground state configurations, while above the blocking point, and capture such configurational changes by cooling back down below the blocking point. So far, this procedure represents the only known way to access local ground state configurations in artificial kagome spin ice and paves the way to explore even more sophisticated annealing procedures that remain to be discovered in future work.

Zusammenfassung

Im Rahmen der vorliegenden Doktorarbeit wurden thermisch induzierte Relaxationsprozesse in zweidimensionalen, frustrierten Nanomagnetarrays untersucht, die häufig auch als *artificial spin ice* bezeichnet werden und hauptsächlich in zwei Geometrien, nämlich im Quadrat (*artificial square ice*) und Kagomegitter (*artificial Kagome ice*) vorliegen. Durch die Anwendung von synchrotronbasierter Photoemissionselektronenmikroskopie konnten die Relaxationsprozesse direkt abgebildet und untersucht werden. Die thermisch induzierte magnetische Relaxation in *artificial spin ice* konnte direkt abgebildet und beobachtet werden, wie *artificial square ice*, das anfangs in einem angeregten Zustand gebracht wurde, durch thermische Relaxation in den Grundzustand bergeht. Durch Vergleich der zeitlichen Evolution des Systems mit Kinetischen Monte Carlo (KMC) Simulationen konnte der Effekt von stochastischen Unregelmässigkeiten der einzelnen Nanomagnete auf den Relaxationsprozess direkt nachweisen.

Ein einfaches Verfahren, bestehend aus einem einmaligen Heizen und Kühlen über und unter der Übergangstemperatur zu thermischen Fluktuationen ($T_B = 320 - 330$ K) war ausreichend, einen langreichweitig geordneten Grundzustand in *artificial square ice* zu erreichen. Dieses stiess jedoch bei *artificial kagome spin ice* an seine Grenzen. Dies wurde bei der Untersuchung sogenannter "Baustein Strukturen" des *artificial kagome spin ice*, bestehend aus bis zu sieben Kagome-Ringen, deutlich. Dabei wuchs die Schwierigkeit des Erreichens der Grundzustände mit wachsender Ring-Anzahl. Schon bei Kagome-Strukturen mit sieben Ringen scheint es unmöglich zu sein, auf diesem Wege Grundzustandskonfigurationen zu erreichen. Eine Extrapolation dieser Erkenntnisse auf unendliche Kagome-Systeme, legt nahe, dass ein langreichweitiger Grundzustand nicht erreicht werden kann, zumindest mit der bis dahin angewandten Methode.

Schliesslich wurden neuere Möglichkeiten zum Erreichen des Grundzustands in *artificial kagome spin ice* untersucht. Durch die Präparation von Kagome-Strukturen mit niedrigerer Übergangstemperatur zu thermischen Fluktuationen ($T_B = 160$ K) sollte erreicht werden, dass T_B unterhalb der theoretisch vorhergesagten Temperaturen für Phasenübergänge liegt. Sowohl kontinuierliches als auch stufenförmiges Kühlen von 370 K zu 140 K brachte jedoch keinen Erfolg. Alternativ, wurde ein Verfahren angewandt, das aus mehrfacher Wiederholung von moderatem Heizen und Kühlen oberhalb und unterhalb von T_B bestand. Diese Prozedur erlaubt es einem Kagome-System im thermischem Gleichgewicht langsame Konfigurationsänderungen durchzuführen, um schliesslich in lokale Minima der Energielandschaft zu fallen, die dann durch das schnelle Kühlen eingefangen werden können. Diese Prozedur ist das bislang einzig bekannte Verfahren, um Grundzustandskonfigurationen in *artificial kagome spin ice* zu erzielen, wenn auch nur lokal und räumlich begrenzt. Es liefert den Grundstein für weiter verbesserte Verfahren, die sicher in naher Zukunft entdeckt werden.

Contents

1	Introduction	13
1.1	From water ice to artificial spin ice	14
2	Experimental Methods	17
2.1	Sample Preparation - Electron Beam Lithography	18
2.1.1	Vistec EBPG5000Plus E-Beam writer	19
2.1.2	E-Beam resist preparation	20
2.1.3	Film deposition via thermal evaporation	20
2.1.4	Lift-off	21
2.2	XMCD/PEEM	22
2.2.1	Synchrotron radiation and the Surface/Interface Microscopy (SIM) beamline at the Swiss Light Source	22
2.2.2	X-ray Absorption Spectroscopy - XAS	23
2.2.3	X-ray Magnetic Circular Dichroism - XMCD	24
2.2.4	Photoemission Electron Microscope - PEEM	25
3	Artificial Square Ice	29
3.1	State of The Art	29
3.2	Geometry & vertex types	30
3.3	Direct observation of thermal relaxation in artificial square ice	32
3.4	Vertex Statistics and the Role of Disorder	34
3.4.1	Kinetic Monte Carlo Simulations and the Role of Disorder	34
3.5	Excitations out of the ground state	37
3.6	Conclusions	40
4	Building blocks of artificial kagome spin ice	41
4.1	State of the Art	41
4.2	Geometry, Energy spectra and low-energy states	42
4.2.1	Simplified Micromagnetic Model	43
4.3	Thickness-Dependent Ordering	45
4.4	Thermally Induced Magnetic Relaxation	48

4.5	Hyper-cubic Energy Landscapes	49
4.6	Correlated Nanomagnet Activity	51
4.7	The Effect of Increasing System Size	55
4.8	Conclusion	56
5	Extended arrays of artificial kagome spin ice	61
5.1	Introduction and Overview	61
5.2	Thermal Relaxation and Emergent Magnetic Monopoles	62
5.2.1	Correlations: Quo Vadis, Ground State?	66
5.3	Towards Optimized Annealing	66
5.3.1	Continuous and Stepped Cooling	69
5.3.2	Cycling around the blocking point	69
5.4	Conclusions	72
6	Summary and outlook	75
6.1	Artificial Square Ice	75
6.2	Artificial kagome spin ice	77

List of Tables

2.1	Electron beam lithography resist parameters.	20
-----	--	----

Chapter 1

Introduction

Relaxation phenomena in various condensed matter systems, including dielectrics [1], glassy systems [2] and proteins [3], have long caught the attention of the research community. While studies of such relaxation processes involved measurements of macroscopic quantities, the recent creation of artificial spin systems, has allowed the dynamics to be inspected microscopically [4, 5]. A prominent example of such systems is artificial spin ice [6] which is considered to be a two-dimensional analogue to the naturally occurring pyrochlore spin ice [7]. Each nanomagnet is monodomain and elongated so that the magnetic moments point in one of two directions parallel to the island long axis, thus mimicking a single Ising spin. The main advantage of artificial spin ice systems is that their geometry can be tailored and their magnetic configurations can be directly visualized and investigated using appropriate imaging techniques [6, 8, 9, 10, 11, 12, 13]. However, due to the high blocking temperatures of the patterned nanomagnets, it has not been possible to observe thermal fluctuations in most of these systems and low energy states could only partially be accessed using demagnetization protocols [6, 9, 10].¹

The ability to pattern and directly investigate thermally active artificial spin ice structures would deliver the perspective to explore relaxation processes and ground state ordering occurring in two-dimensional frustrated systems. Therefore, the main goal of the presented work was to obtain artificial spin ice structures with fluctuating magnetic moments, ideally at temperatures that would be accessed easily, without causing either sample damage or any experimental difficulties, and to investigate thermally driven magnetic relaxation processes occurring in artificial spin ice systems, both in the square and kagome lattice geometry. Being essential for the further understanding of the presented work, the following sections will introduce the reader to some fundamental properties of frustration, Pyrochlore spin ice and artificial spin ice.

¹Text taken from our publication [25].

1.1 From water ice to artificial spin ice

Frustration is a phenomenon that arises when competing interactions within a system can not be satisfied at the same time, leading to highly degenerate low-energy states. Systems incorporating frustration have long captured the interest of the scientific community, due to their fascinating behavior including spin freezing phenomena [14, 15], and history dependent relaxation processes [16, 17], but also because the understanding of their behavior leads to the interpretation of related complex systems. For example, spin-glass models, derived from extensive experimental research, have found their way into various other fields, providing a basis for modeling neural networks [18] and protein dynamics [19], and the generation of error-correcting codes [20].

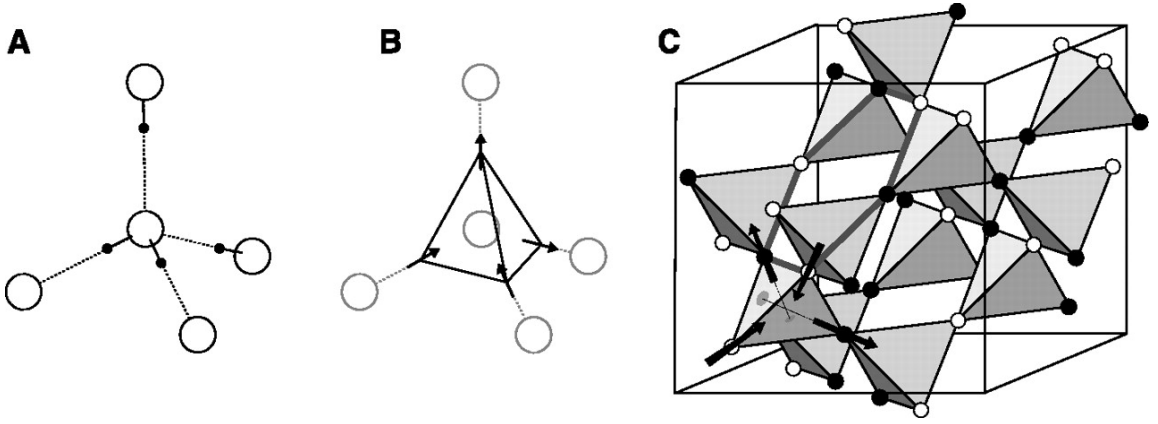


Figure 1.1: **(A)** Proton ordering in water ice, obeying the so-called ice rules. Each oxide ion (large white circles) is tetrahedrally coordinated with four other oxide ions, with two near and two further sited protons (small black circles). **(B)** Ice rule analogue achieved in pyrochlore spin ice. Two moments point towards and two point out of the center of the tetrahedra. **(C)** Pyrochlore $Ho_2Ti_2O_7$ crystal structure of corner-sharing tetrahedra. Figure taken from [21].

Geometric frustration is a particular case where both the lattice geometry and the magnetic interaction are responsible for the frustration. Historically, the first ever known example of geometric frustration was identified in water ice, which exhibits frozen-in disorder remaining down to ultra-low temperatures, and therefore a residual entropy [22]. This led to the prediction of a certain type of proton-disorder [23] in water ice that obeys the so-called Bernal-Fowler "Ice Rule" [24]. This rule requires two protons to reside near the oxide ion and two further away from it [see Fig. 1.1a].

Regarding magnetic systems, it has long been thought that geometric frustration can not occur when interactions are purely ferromagnetic until the discovery of geometrical frustration in ferromagnetic pyrochlore $Ho_2Ti_2O_7$, widely known as spin ice [7]. Here, the

Ho^{3+} ions occupy a pyrochlore lattice of corner-sharing tetrahedra with the oxide ions occupying the centres of the tetrahedra, so that two Ho^{3+} ions will reside closer to the oxide ion along the $[111]$ -direction than the other two. These crystallographic environment forces the Ho^{3+} moments to point either towards or out of the centres of the corner-linked tetrahedra [see Fig. 1.1b and c]. Such ferromagnetically coupled Ising spins, residing at the corners of a tetrahedron possess a ground state configuration that will have two moments pointing in and two moments point out of the centre. This two-in-two-out condition is an analogue to the aforementioned proton ordering occurring in water ice [22, 23] and is why the term "spin ice" has been introduced.

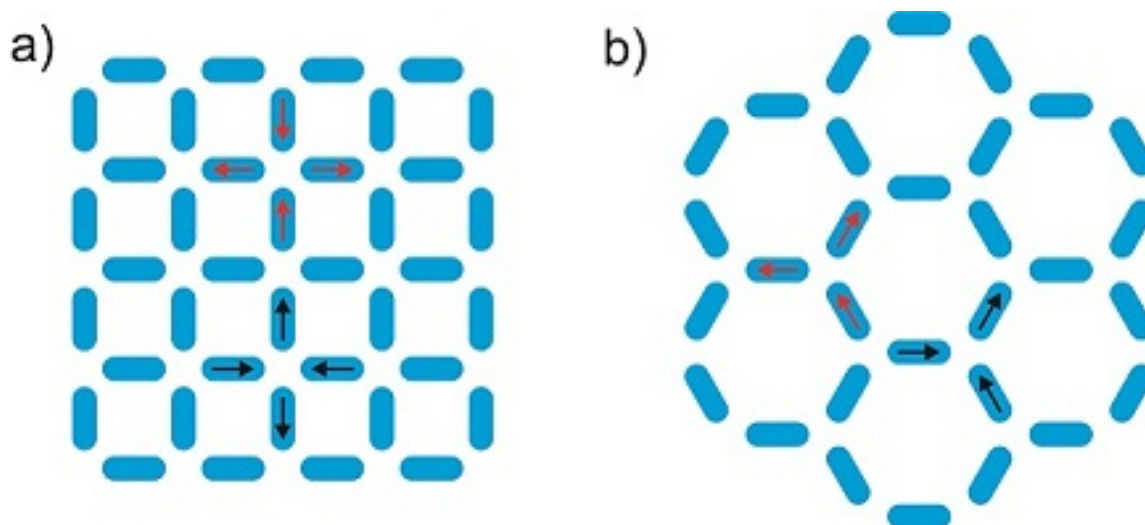


Figure 1.2: Artificial spin ice. **(a)** Artificial square ice, where nanomagnets occupy the sites of a square lattice. Dipolar coupling favors a moment configuration of two moments pointing in and two moments pointing out of a vertex where four nanomagnets meet. **(b)** Artificial kagome spin ice, where nanomagnets occupy the sites of a kagome lattice, giving a honeycomb structure. The ice-rule is defined by two-in-one-out (black arrows) or one-in-two-out moment configurations at the vertices (red arrows).

In recent years, extensive efforts have been directed towards the investigation of artificial spin ice systems [6], comprising ferromagnetic nanoislands arranged in two dimensional geometries, such as artificial square ice [6, 8], where the nanomagnets occupy the sites of a square lattice [see Fig. 1.2a]. Each nanomagnet is small enough to be monodomain and elongated, so that the shape anisotropy forces the magnetization to point along the long axis, thus mimicking a single Ising-like macrospin. As these nanomagnets are dipolar coupled, neighboring pairs will have their moments preferably aligned head-to-tail, leading to moment configurations of two moments pointing in and two moments pointing out of a vertex where four nanomagnets meet [see Fig. 1.2a]. Therefore, these systems are

considered to be two dimensional analogues to Pyrochlore spin ice, but possess the main advantage that their configurations can be directly visualized, using appropriate imaging techniques such as magnetic force microscopy (MFM) [6, 12], Lorentz microscopy [9] or photoemission electron microscopy (PEEM) [10, 13, 5, 25]. We will turn our focus to artificial square ice in more detail in the third chapter of this work.

Besides artificial square ice, another artificial spin ice system exists, named artificial kagome spin ice, where the nanomagnets occupy the sites of a kagome lattice, thus giving a honeycomb structure as seen in Fig. 1.2b. The ice-rule here is manifested by two-in-one-out or one-in-two-out moment configurations at each vertex where three nanomagnets meet [26] [see Fig. 1.2b]. Such a kagome spin ice phase arises in Pyrochlore spin ice, when a magnetic field is applied along the [111] direction [27]. Artificial kagome spin ice will be the main focus of the fourth and fifth chapter in this work.

Chapter 2

Experimental Methods

Before discussing the details of thermal relaxation processes observed in artificial spin ice systems, it is important to give the reader an overview on the experimental methods used to accomplish the work presented here, ranging from sample fabrication using lift-off assisted electron beam lithography to magnetic characterization via synchrotron based photoemission electron microscopy (PEEM).

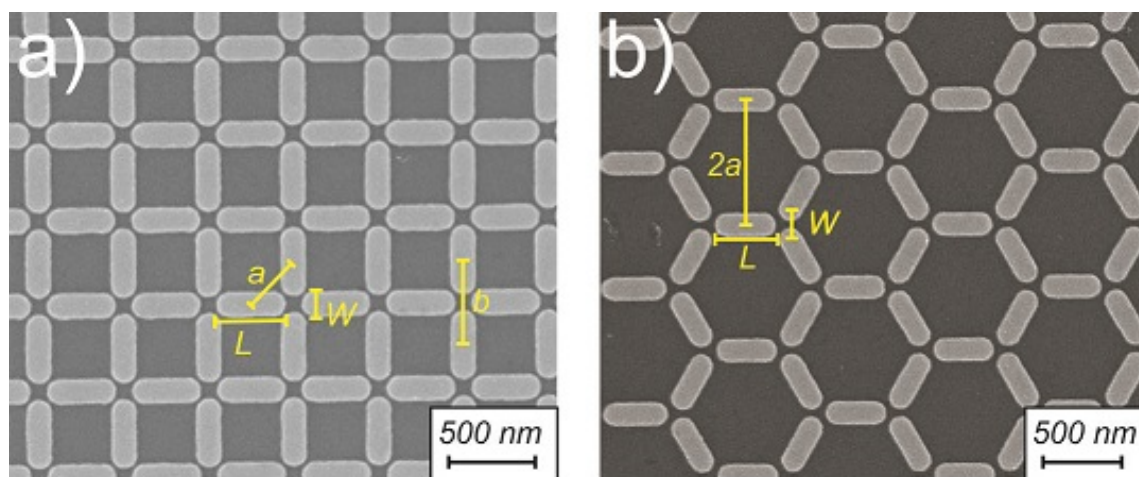


Figure 2.1: Lithographically patterned artificial spin ice structures. **(a)** SEM image of an artificial square ice array with a nanomagnet length $L = 470$ nm, width $W = 170$ nm and a lattice constant $a = 425$ nm. **(b)** SEM image of an artificial kagome spin ice array with the same length and width of the nanomagnets and a lattice constant $2a = 1000$ nm.

2.1 Sample Preparation - Electron Beam Lithography

We used electron beam lithography in order to obtain artificial spin ice structures as shown in Fig. 2.1. For both artificial square ice and artificial kagome spin ice structures the arrays consisted of elongated nanomagnets placed on a silicon substrate. The sample fabrication

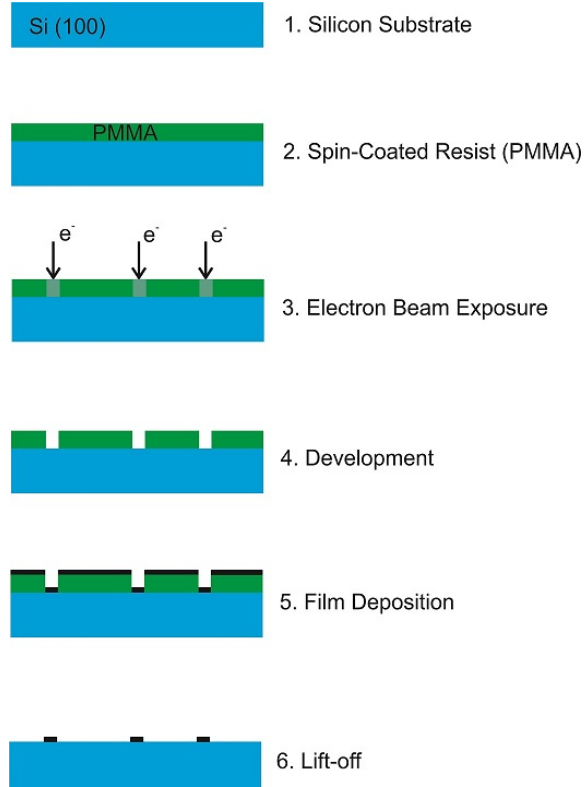


Figure 2.2: Fabrication steps.

steps [see Fig. 2.2] can be broken down into two major parts, namely the patterning of a polymer resist and the transferring of the achieved pattern to a ferromagnetic thin film material. The first part consists of developing an electron beam exposed polymer resist layer (typical resist layer thickness: 70 nm), spin coated on a silicon substrate [see Fig. 2.2 steps 1-4]. After development, the exposed area is removed and the pattern transfer is performed in the second step of sample fabrication, where we use thermal evaporation to deposit a magnetic thin film onto the substrate, which is followed by lift-off in acetone [see Fig. 2.2 steps 5-6]. In the lift-off process all unwanted resist and magnetic material on top is removed [see Fig. 2.2 step 6]. The details of the fabrication process are given in the following subsections.

2.1.1 Vistec EBPG5000Plus E-Beam writer

An electron beam lithography system [see Fig. 2.3] uses focused electron beams to pattern structures in an electron sensitive resist. The electron beam is scanned across the wafer using electromagnetic defelection systems. At the Laboratory for Micro- and Nanotechnology (LMN), Paul Scherrer Institute, we use a Vistec EBPG5000Plus electron beam writer, which features a vector scan system to deflect the beam only to areas needed to be exposed with "trapezium" shape fill-in using a spot beam with Gaussian distribution, with a minimum spot size of around 5 nm. The main advantage of electron beam lithography is a high resolution and the possibility to perform multiple exposures with precise overlay, flexibility and placement. We are able to pattern all structures we need for an experiment directly on one substrate.

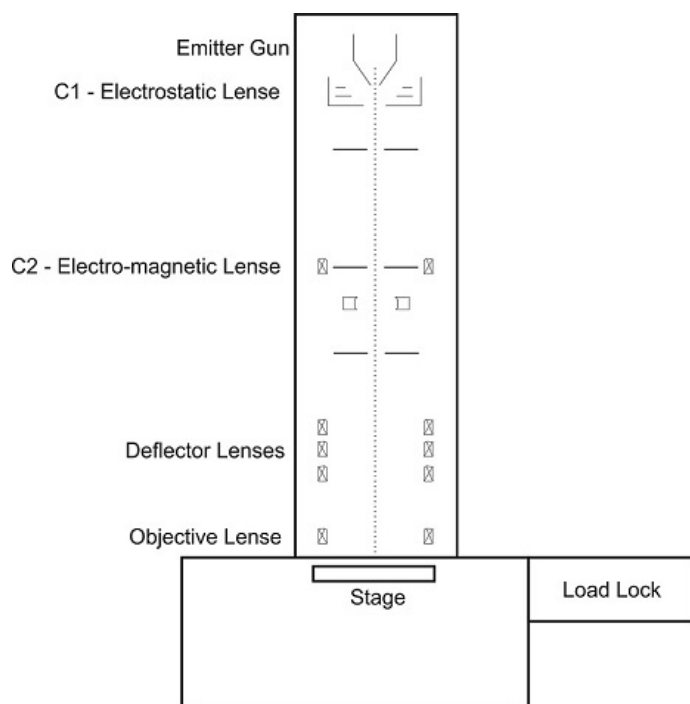


Figure 2.3: Schematics of an electron beam lithography writer. Electrons are emitted from an emitter gun. The beam current and spot size are then controlled via lenses C1 and C2. The defelection system moves the beam to the correct area on the substrate to write the patterns. The final focus of the beam onto the sample is then performed via an objective lens.

Resist Layer Parameters	
Substrate	Si (100) chip 1 cm \times 1 cm
Resist	PMMA 950 k 2% Ethyl Lactate (EL)
Resist thickness	70 nm
Velocity	4000 rpm
Acceleration	3000 rpm/s
Time	45 s
Baking	2 minutes at 170°
Developer	45 seconds MIBK:IPA 1:3

Table 2.1: Electron beam lithography resist parameters.

2.1.2 E-Beam resist preparation

One of the main requirements for electron beam lithography is the ability to prepare resist layers of reproducibly uniform and well-specified thicknesses. We use a spin-coater to obtain such resist layers of constant thickness on top of $1 \times 1 \text{ cm}^2$ silicon substrate. A drop of thinned resist is placed on top of the substrate, and immediately distributed by rotating the substrate at high speeds. Four main factors determine the layer thickness achieved after spin coating: the concentration of the resist in the solution, the rotation speed, acceleration and the spin time. Immediately after spin-coating, the sample is put on a hot plate for baking. The baking temperature of 170° C is chosen, so that it is above the boiling temperature of the solvent, in order to outgas any remaining solvent from the resist. The temperature is also above the glass transition temperature of the polymer, so that it is transformed from a polycrystalline state to an amorphous one, thus giving a smoother surface. Overall, the spin coating parameters used in this work are summed together in Table 2.1.

Using a positive exposure definition with Polymethyl Methacrylat (PMMA) resist, the electron beam exposed regions will be removed in an appropriate developer. We used PMMA resist with 950k molecular weight dissolved in ethyl lactate (EL). The development was performed using a HAMATECH (steag-Hamatech HME 500) developing machine, which gives a fully automated and reproducible developing process. While rotating at moderate speed, the sample is sprayed with a developer (1:3 MIBK:IPA), providing a uniform spreading of the developer on the exposed resist. This is set for 45 seconds. Then, the developer is rinsed away by spraying pure isopropyl alcohol (IPA) and finally, the sample is dried by high speed rotation.

2.1.3 Film deposition via thermal evaporation

Thermal evaporation of Permalloy (Ni83%Fe17%) is the main deposition method used for the current work. A Balzers BAE250 coating system is used with a special sample holder,

that can be moved manually beneath a fixed shutter [see Fig. 2.4]. The main goal using this setup is to create a permalloy wedge film, allowing us to vary the energy barriers for thermally driven moment reorientation of the patterned nanomagnets. Evaporation was performed at a base pressure of 6×10^{-6} mbar and an evaporation pressure of 6×10^{-5} mbar. The thermal source is a Tungsten boat heated up to a temperature around 1100° C. On top of the Permalloy wedge film, an Aluminum capping layer of 2 nm is deposited, in order to prevent fast oxidation outside the vacuum. An atomic force microscope (AFM) was used to determine the deposited and patterned film thicknesses.

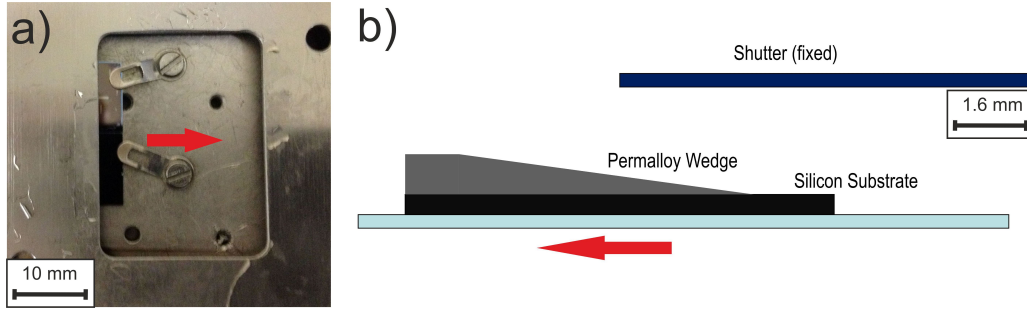


Figure 2.4: Wedge film deposition set up. (a) Image of the sample holder with two electron beam exposed and developed substrates placed beneath a fixed shutter window. During film deposition, the holder is moved manually into the shutter window (red arrows), thus creating a wedge film. (b) Schematic of wedge sample fabrication.

2.1.4 Lift-off

Following Permalloy wedge film deposition, all unwanted magnetic material and resist film is removed with the lift-off process, using acetone as a solvent. Unexposed PMMA dissolves in acetone, while the deposited metal in contact with the silicon substrate is not removed during the lift-off process. The acetone used is required to fulfill high purity standards, in order to achieve a clean lift-off. Therefore, the substrate is placed in a beaker filled with high quality MOS Acetone in an ultra-sound bath. In order to maintain a clean lift-off, as magnetic material is subsequently removed, it is important to replace acetone every 5-10 minutes. This procedure is repeated up to 5 times, depending on the progressing lift-off process. During the acetone change, it is important to keep the substrate from getting dry, as this would result in adhesion of unwanted magnetic material onto the substrate. This procedure is followed by putting the substrate into a beaker filled with MOS isopropyl alcohol (IPA), in order to remove the acetone. The beaker is again placed into an ultra-sound bath for a period of 2-3 minutes. Then, the sample is dried with a nitrogen gas gun. Following the lift-off, an SEM inspection is performed, in order to check the final quality of the sample and provide a measurement of the nanomagnet dimensions (length and width).

2.2 XMCD/PEEM

After going through the details of sample fabrication, we want to turn our focus now to the main magnetic sample characterization technique used for this work, namely X-ray photoemission electron microscopy (PEEM), taking advantage of the X-ray magnetic circular dichroism effect (XMCD) at the Fe L_3 edge [29]. XMCD/PEEM imaging is the ideal technique to investigate artificial spin ice structures, both the kagome geometry [10, 13, 30, 5], as well as in the square lattice geometry [25], because of the easy visualization of the magnetic moment of all the nanomagnets within an array with a single image. Beside this, it delivers a high spatial resolution and an acquisition time of a few seconds, allowing a direct investigation of thermal dynamics of artificial spin ice in real space and time [5, 25].

2.2.1 Synchrotron radiation and the Surface/Interface Microscopy (SIM) beamline at the Swiss Light Source

Synchrotron light sources possess the ideal properties in order to perform X-ray based spectroscopy and microscopy, as they provide wide-range of tunable X-ray energies, and a relative fast switching of X-ray polarization. A major part of the XMCD/PEEM measurements presented in this thesis were performed at the Surface/Interface Microscopy (SIM) beamline at the Swiss Light Source (SLS) [28]. The SLS is operated by the so-called top up mode, which guarantess a constant value of current (approx. 400 mA) in the storage the ring. Electrons are extracted and accelerated in a LINAC and a booster ring, and then injected into the storage ring. In the storage ring, they are kept in a closed path using bending magnets at arc sections. The energy of the electrons inside the storage ring of the SLS is 2.4 GeV. Ultra high vacuum conditions are required to achieve an electron velocity very close to the speed of light. Then, the beamlines use the radiation emitted from accelerating electrons passing through insertion devices, such as wigglers, undulators or bending magnets. The photon energy of the SIM beamline ranges from 90 eV up to 2000 eV [31]. The beamline consists of two 3.8 m long undulators as insertion devices, located one behind the other (see Undulator 1 and Undulator 2 in Fig. 2.5), followed by a collimating mirror directly after the shielding wall, a plane grating monochromator and focusing mirrors [32, 31]. Measurements with circularly polarized light (left and right) and linearly polarized light are possible. A fast switching of polarization is made possible, using the so-called *tune-detune* undulator mode (see Fig. 2.5). This involves the *tuning* of the energy of one of the two undulators to match the small energy band pass of the monochromator (width \sim meV), so that X-rays with a certain polarization are delivered to the experiment. Meanwhile, the second undulator is *detuned* by changing the gap by a few millimeters, which will shift the center of the emitted photon energy away from the energy band pass of the monochromator such that nearly no intensity from the *detuned* undulator goes through [31].

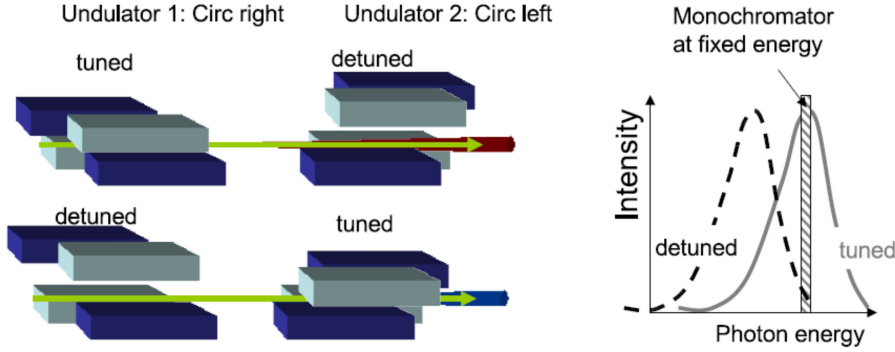


Figure 2.5: Polarization switching with the *tune-detune-scheme*. The photon energy generated from one of the two undulators has a narrow bandwidth in the range of a few electron-volts, and must be *tuned* to match the monochromator energy, in order to get photons on the sample. The energy of the the *detuned* undulator will not match the monochromator energy, so that no photon will hit the sample. Figure adapted from [31].

2.2.2 X-ray Absorption Spectroscopy - XAS

In X-ray absorption spectroscopy (XAS), core-level electrons are excited into unoccupied states above the Fermi level by incident X-rays. Depending on the involved energy ranges, XAS can be categorized into two regimes. The first deals with resonances near absorption edges and is called X-ray absorption near edge spectroscopy (XANES) or near edge X-ray absorption fine structure (NEXAFS). XANES (or NEXAFS) contains information about the unoccupied electronic states and the chemical environment [33, 34]. The second type of spectroscopy is called extended x-ray absorption fine structures (EXAFS) and deals with energies that are above the absorption edges. EXAFS is used to determine the type and distance of atoms in the local environment of the absorbing atom [34]. Here, we are concerned with X-ray absorption near edge structure (XANES), as it is relevant for imaging.

The intensity of X-rays passing through matter of thickness d can be calculated by the Lambert-Beer equation:

$$I(E, x) = I_0(E) \exp[-\mu(E) \cdot d] \quad (2.1)$$

μ being the photoabsorption coefficient. For energies below 20 keV, the photoeffect is the most dominant type of interaction between photons and electrons. μ is proportional to the absorption cross section σ_{abs} , which is the transition probability P_{fi} per unit time for a photon flux I_{ph} :

$$\mu \propto \sigma_{abs} = P_{fi}/I_{ph} \quad (2.2)$$

The transition probability P_{fi} can be derived using Fermi's golden rule:

$$P_{fi} \propto \sum_{f,i} M_{f,i}^2 \cdot (1 - n(E_f)) \cdot \delta(\hbar\omega - (E_f - E_i)) \quad (2.3)$$

$(1 - n(E_f))$ being the density of unoccupied final states. The δ -function takes the energy conservation into account. Within an electric dipole approximation, the transition matrix element $M_{f,i}^2$ is given by $|\langle f | P \mathbf{A} | i \rangle|^2$, where P is the momentum vector and \mathbf{A} the propagation vector of the electric field containing the polarization of the X-rays. Within the dipole approximation, transitions are allowed according to the dipole selection rules:

$$\Delta m_s = 0, \Delta m_l = \pm 1 \quad (2.4)$$

For example, transitions from the 2p to d states within $L_{3,2}$ absorption edges are allowed. Also included within the dipole approximation are transitions from 1s to p states within the K absorption edge.

There are three ways to measure absorption spectra, the first being the measurement of the transmitted photon intensity going through the sample normalized to the incoming photon intensity. The other two methods are X-ray fluorescence, which works better in the hard X-ray regime, and total electron yield (TEY), which is situated in the soft X-ray regime. Here, the absorption of X-rays leads to the creation of holes, which are then filled via the emission of Auger electrons. The emitted Auger electrons cause a low-energy cascade of electrons at the sample surface [see Fig. 2.6] with a mean free path way of 7-9 nm. Only electrons that escape the sample surface contribute to the total electron yield.

2.2.3 X-ray Magnetic Circular Dichroism - XMCD

X-ray magnetic circular dichroism (XMCD) is the effect that the absorption of circularly polarized X-rays depends strongly on the relative orientations of the photon helicity and the magnetization of the absorbing magnetic material. For example, if an X-ray photon with a positive helicity is absorbed by an electron from a spin-orbit-split core level ($2p_{3/2}$ and $2p_{1/2}$), excitations, with their related probabilities, and while obeying selection rules, will yield an orbital polarization of excited electron states. From the $2p_{3/2}$ state, 62.5% excited electrons will be spin-up electrons, and only 37.5% spin-down electrons. From the $2p_{1/2}$ state, 75% excited electrons will be spin-down, while 25% will be spin-up electrons [see Wende et al. in [34]]. For X-ray photons of negative helicity the results will be exactly reversed.

XMCD is defined as the relative division of X-ray absorption with circular right (σ^+) and circular left (σ^-) polarization:

$$\frac{\sigma^+ - \sigma^-}{\sigma^+ + \sigma^-} \quad (2.5)$$

If one would now obtain images with two opposite circular polarized X-rays (σ^+ and σ^-), the resulting dark and bright contrast in an XMCD image is a measure of the angle α

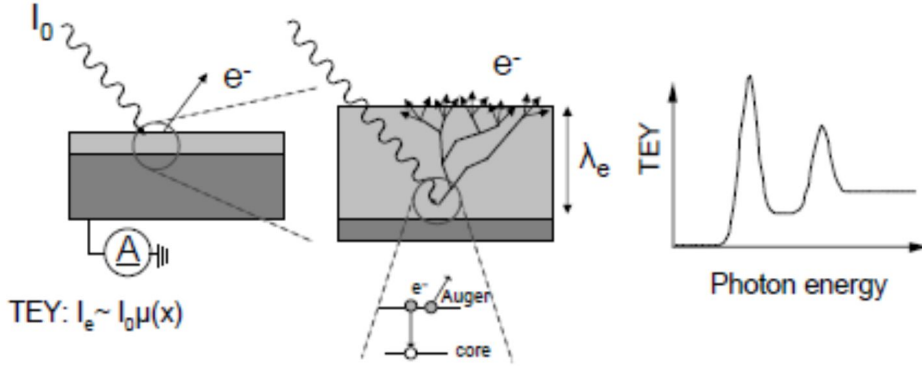


Figure 2.6: X-ray absorption process and total electron yield geometry (TEY). Absorbed X-rays lead to the creation of Auger electrons, which themselves lead to a cascade of electrons escaping the sample. The number of emitted electrons is proportional to the probability of Auger electron creation (absorption coefficient). Therefore, the TEY is proportional to the absorption coefficient, and exhibits maxima at the absorption edges. Figure adapted from [33].

between the circular X-ray polarization vector $\vec{\sigma}$ and the magnetization \vec{M} [34, 35]. This is given by:

$$I_{XMCD} = \vec{M} \cdot \vec{\sigma} = |\vec{M}| \cos(\alpha) \quad (2.6)$$

Maximum XMCD contrast is obtained if magnetization and the X-ray polarization vector are parallel to each other. When designing our artificial spin ice structures, it is therefore important to make sure all patterned nanomagnets will have their magnetic moments with non-zero projections along the incoming X-ray direction.

2.2.4 Photoemission Electron Microscope - PEEM

In a photoemission electron microscope (PEEM), electrons emitted from a sample in response of the X-ray absorption are recorded. Electrons escaping the sample surface are accelerated by a strong electric field between the sample and the objective lens [see Fig. 2.7a], followed by a series of magnetic or electrostatic electron lenses, thus creating a hundred- or thousand-fold magnified image of the investigated structure. In combination with the aforementioned tune-detune mode to switch X-ray polarizations, we are able to obtain XMCD images in time scales of 8-10 seconds [5, 25]. In addition, using a single-polarization imaging mode [Fig. 2.7b], we are able to investigate dynamics that occur on a timescale of a few hundreds of milliseconds [5].

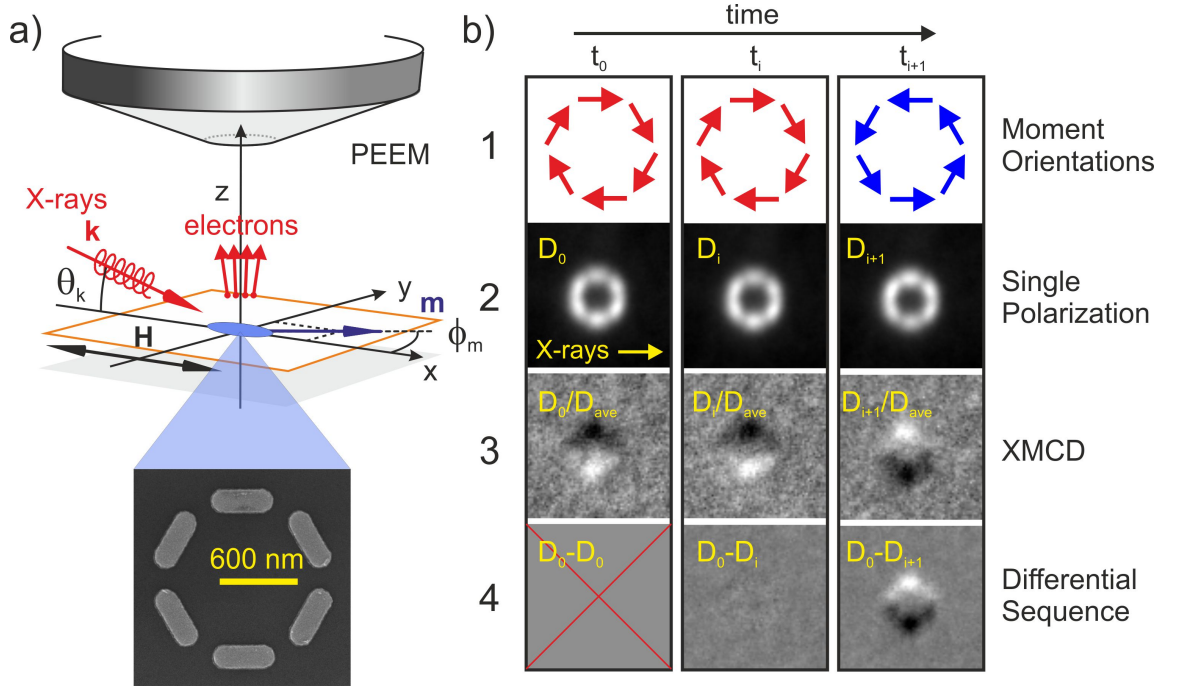


Figure 2.7: (a) Schematic of a PEEM measurement, where the sample is illuminated with circularly polarized X-rays (incoming angle $\theta_k = 16^\circ$) and the imaging of the excited secondary electrons reveals an intensity map proportional to the local X-ray absorption cross section. Below this schematic is a scanning electron microscope image of a typical kagome single ring. The XMCD effect leads to a magnetization-dependent intensity of each island (see Eq.2.6). (b) Panel 1: schematics of a dynamic sequence of low-energy states of the single-ring kagome system at times t_0, t_i and t_{i+1} . Panel 2: the corresponding sequence of images D_0, D_i and D_{i+1} obtained with PEEM when illuminating with a fixed circular polarization. Magnetization reversal of the nanomagnets leads to correspondingly altered intensities in the images. Pixelwise division of individual images by the averaged imaged of the whole sequence delivers the corresponding XMCD contrast images in panel 3. Subtracting the first image of the sequence from the other images deliver the differential XMCD images seen in panel 4. Figure adapted from [5].

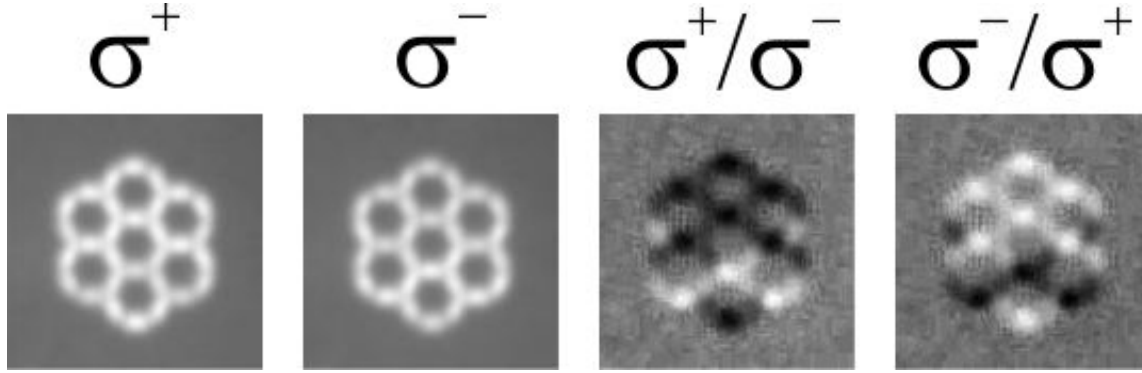


Figure 2.8: XMCD image acquisition at the Fe L_3 edge. Absorption images are recorded at the Fe L_3 edge with right and left circularly polarized X-rays. Pixelwise division of the absorption images delivers XMCD images with enhanced contrast.

Imaging and Heating/Cooling measurements with PEEM

The major part of PEEM measurements discussed in chapters 3-5 were performed in a classical two polarization XMCD imaging mode. This involves recording images with circular right and circular left polarized light. Pixelwise division of the obtained images ($\frac{\sigma^+}{\sigma^-}$) delivers XMCD contrast images [see Fig. 2.8]. For image acquisition, we chose for each polarization an exposure time of one second, which is averaged 3-4 times and, taking the time needed for a polarization switch (1-2 seconds) into account, we obtain XMCD image sequences within a time frame of 7-10 seconds per image. As we will see in the following chapters, this time scale proved to be sufficient for direct observations of thermally activated moment reorientations in the patterned nanomagnets [5, 25]. At higher temperatures, giving higher fluctuation rates, a single-polarization imaging mode was applied [5] [see Fig. 2.7], allowing us to observe thermally driven dynamics in time scales of 300-700 ms.

Regarding the capability of cooling down well below room temperature, PEEM faces issues with vibrations and thermal drift. Besides that, the SLS PEEM lacks a real temperature control. The major complexity is that PEEM is designed with the sample at high voltage of up to 20 kV, meaning that one must cool the sample while maintaining electrical isolation between the sample and the cryostat.

PEEM3 at the Advanced Light Source (ALS)

Due to the aforementioned limitation of the cooling/heating possibilities of the PEEM at the Swiss Light Source, we performed additional measurements at the 11.0.1 beamline (PEEM3) at the Advanced Light Source (ALS), where a special cooling/heating setup allows not only for a fast and stable temperature control, but also the possibility to cool down to temperatures around 20 K [36]. The setup includes a cryostat with its cold head

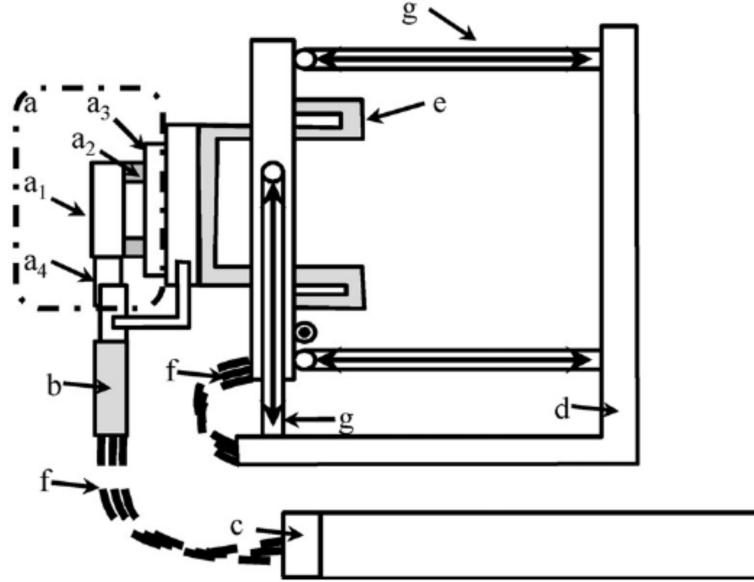


Figure 2.9: Schematic of the special cooling setup of PEEM3 at the Advanced Light Source showing the main components: (a) removable cryogenic sample puck, consisting of copper sample mounting block (a1), thermally isolating mechanical connections (a2) to baseplate (a3) and silicon thermal interface nose (a4). (b) Electrically isolating, thermally conducting sapphire rod. (c) Cold head of helium cryostat. (d) Electrically and thermally grounded manipulator base. (e) Electrically isolating insulator. (f) Flexible and thermally conductive copper braid. (g) flexural push rods. Schematic and description adapted from [36].

attached to the moving manipulator sample dock first through a flexible copper braid to decouple it from the sample motion and minimize possible vibration transmission. Thermal conductivity is maintained by a sapphire rod at the end of the copper braid, while securing electrical isolation of the 20 kV sample dock from the grounded cryostat. The sapphire is then attached to a block of gold coated copper ribbons that are part of a clamping mechanism, which allows the thermal connection to the special cold sample holder [36] [see Fig. 2.9]. PEEM3 not only gives the possibility to cool down to temperatures around 20 K, but also provides us with a full temperature control and stable temperature conditions.

Chapter 3

Artificial Square Ice

We turn our focus now to the results obtained by investigating thermally driven magnetic relaxation in artificial square ice. We investigate the thermal relaxation with PEEM, and are able to directly observe how such a system finds its way from an energetically excited state to the ground state. On plotting vertex type populations as a function of time, we can characterize the relaxation, which occurs in two stages, namely a string and a domain regime. Kinetic Monte Carlo simulations agree well with the temporal evolution of the magnetic state when including disorder, and the experimental results can be explained by considering the effective interaction energy associated with the separation of pairs of vertex excitations [25]. The results and text presented in this chapter are partly adapted from our recent publication [25].

3.1 State of The Art

Up to the starting point of this project, most artificial square ice systems were patterned from permalloy or cobalt films with thicknesses between 20 and 30 nm. In this thickness range the magnetic moments are static and the majority of experiments have focused on field driven processes such as so-called demagnetizing protocols that involved rotating a sample in a decreasing magnetic field in order to achieve low energy configurations [6, 11], with the result that long range ordered ground state configurations could not be accessed. In order to achieve an improved analogue to the bulk spin ice, one of the key goals in the field has been to realize and investigate thermally active artificial spin ice. Morgan et al. [8] observed that a long-range ordered state can be accessed in an as-grown artificial square ice, indicating that the ordering process occurs during the early stages of film deposition. This suggests the possibility to obtain a thermally active artificial spin ice in ultra-thin films and in recent work on patterned ultra-thin Fe films [48], it was shown how remanent configurations of artificial square ice, which are frozen at low temperatures, started to “melt” with increasing temperature via thermally induced moment reorientations

in the nanomagnets. Rather than “melting” artificial square ice, we would ideally obtain a thermally activated artificial square ice system with strong inter-island dipolar coupling. Such a system will ideally relax to one of two degenerate ground states. The best way to do that was achieved by patterning a Permalloy (Ni80%Fe20%) wedge film [see Fig. 2.4]. This approach allows us to vary the energy barriers for thermal fluctuations, so that quasi-static states are achieved at higher thickness while thermally driven moment re-orientations occur at lower thicknesses [5, 25, 51].

3.2 Geometry & vertex types

Artificial spin ice, consisting of nanomagnets arranged in two-dimensional frustrated geometries was first proposed in the square lattice geometry [6], where the patterned nanomagnets occupy the sites of a square lattice [see Fig. 3.1]. As the nanomagnets are dipolar coupled, neighboring pairs, in a low-energy configuration, will have their moments aligned head-to-tail, thus giving a two-in-two-out moment configuration at each vertex where four nanomagnets meet. Therefore, artificial square ice was introduced to be a two-dimensional analogue to pyrochlore spin ice [7]. While there are six possible vertex configurations that obey the so-called ice rule (two-in-two-out), in artificial square ice, they are not all energetically equivalent [6, 37]. This is a result of non-equal inter-nanomagnet distances at each vertex where four nanomagnets meet [see a_1 and b_2 in Fig. 3.1a]. This results in the existence of a ground state configuration (Type I vertices) that is energetically clearly separated from the higher energy configurations (Type II-IV). A consequence is also a strong confining/deconfining potential in artificial square ice [42, 25].

We define each nanomagnet to have either one of two possible magnetic states with the moments aligned along the long axis of the nanomagnets. Then, as mentioned before, these magnetic moments interact via the magnetic dipolar interaction:

$$V(\mathbf{r}_{ij}, \mathbf{m}_i, \mathbf{m}_j) = -\frac{\mu_0}{4\pi r_{ij}^3} [3(\mathbf{m}_i \cdot \hat{\mathbf{r}}_{ij})(\mathbf{m}_j \cdot \hat{\mathbf{r}}_{ij}) - \mathbf{m}_i \cdot \mathbf{m}_j] \quad (3.1)$$

where \mathbf{r}_{ij} is the distance vector separating the i th and j th nanomagnets with magnetic moments \mathbf{m}_i and \mathbf{m}_j . Calculating configurational energies, the vertex type may be classified into four different types with increasing dipolar energy (Type I to Type IV) (see Fig. 3.1c). The lowest energy configuration in an artificial square ice consists of an array of Type I vertices, resulting in alternating clockwise and anticlockwise vortex plaquettes (see Fig. 3.1b). This ground state has a degeneracy of two, which can give rise to domains of opposite chirality separated by domain boundaries [8, 25]. Type II vertices also obey the ice-rule, but have a higher energy since the interactions between the nanomagnets at a vertex in these two-dimensional systems are not equivalent [6, 37]. In a Type II vertex, all four neighboring nanomagnets point towards the same direction (see Fig. 3.1c). Type III vertices can be considered as mobile vertex defects, which, through their migration, mediate configurational changes. Type IV vertices have all moments pointing in or all moments

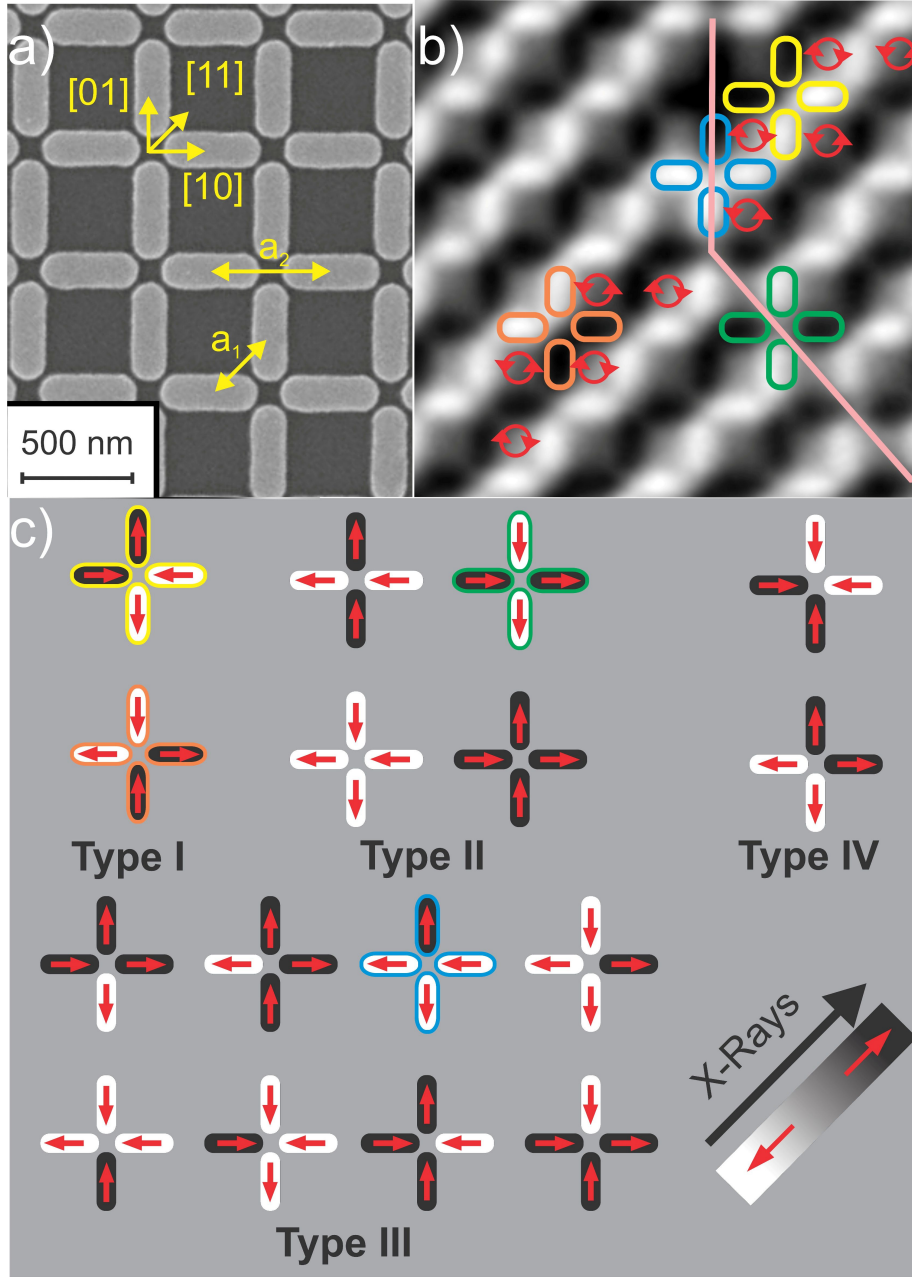


Figure 3.1: Artificial Square Ice. (a) SEM image and (b) XMCD image resolving vertex type configurations detailed in (c). Highlighted in orange and yellow are Type I vertices, and green and blue are a Type II and a Type III vertex, respectively. Present are two Type I ground state domains of opposite chirality separated by a domain boundary (pink line) consisting of Type II and Type III vertices. Figure adapted from [25].

pointing out, and represent the most energetic configuration, which is never observed in our experiments [25]. These vertex types and their statistics at a given time are a nice way to characterize an artificial square ice system energetically, which is essential to understand the undergoing relaxation process [25].

3.3 Direct observation of thermal relaxation in artificial square ice

As mentioned in the experimental methods, we patterned a Permalloy (Ni83%Fe17%) wedge film on a silicon (100) substrate using electron beam lithography. Artificial square ice arrays consisting of nanomagnets, with length $L = 470$ nm, width $W = 170$ nm and nearest-neighbor center-to-center distance $a = 425$ nm, were fabricated, ranging in thickness from 0 to 15 nm over a distance of 3 mm, with a 3 nm-thick aluminum capping layer. Varying the film thickness allows us to vary the energy barrier for thermal fluctuations and perfectly match the moment reorientation rates with the temporal resolution of XMCD imaging with PEEM, which is roughly 7-9 seconds per image. A film thickness of 3 nm and a temperature of $T = 350$ K was found to be ideal to observe the full relaxation process [25].

An array of Type II vertices was created in the artificial square ice after application of a saturating magnetic field (35 mT) along the negative [11]-direction, and image acquisition was begun immediately after the magnetic field was switched off. Initially, all moments point towards one direction [see bright XMCD contrast in Fig. 3.2a-c]. Then, while undergoing thermal relaxation from a 100% Type II vertex configuration, down to one of the two ground state configurations (Type I vertex configuration), the system was found to go through two main regimes. During the first regime we see isolated chains of Type I vertices emerge within a Type II vertex background via the creation of Type III vertex pairs and their separation [see Fig. 3.2a-d]. Since this involves neighboring reversed island moments appearing as black lines, we refer to this regime as the string regime [see Fig. 3.2a-d]. During the string propagation, the reversal of nearest neighbor moments (in orthogonal nanomagnets) creates a chain of Type I vertices within the initially saturated Type II background. In addition, the moment reversal of next-nearest neighbor nanomagnets creates Type II vertices of a different kind [see Fig. 3.1c and Fig. 3.3a]. These Type II vertices will later form part of the domain boundaries in the domain regime [see Fig. 3.3b]. With an increasing number of strings, the ends of the strings meet in either the same or across adjacent rows, and eventually form areas of (lowest energy) Type I vertices. As there are two possible orientations for the Type I vertex [8], such Type I areas can be divided into two domain types of opposite chirality [see Fig. 3.1b]. This stage marks the beginning of the domain regime [see Fig. 3.2e-g]. In this domain regime, Type I domains of opposite chirality, separated by Type II boundaries, evolve via Type III vertex creation and propagation along the domain boundaries [see Fig. 3.2e-g and Fig. 3.3b]. As a result of

3.3. DIRECT OBSERVATION OF THERMAL RELAXATION IN ARTIFICIAL SQUARE ICE33

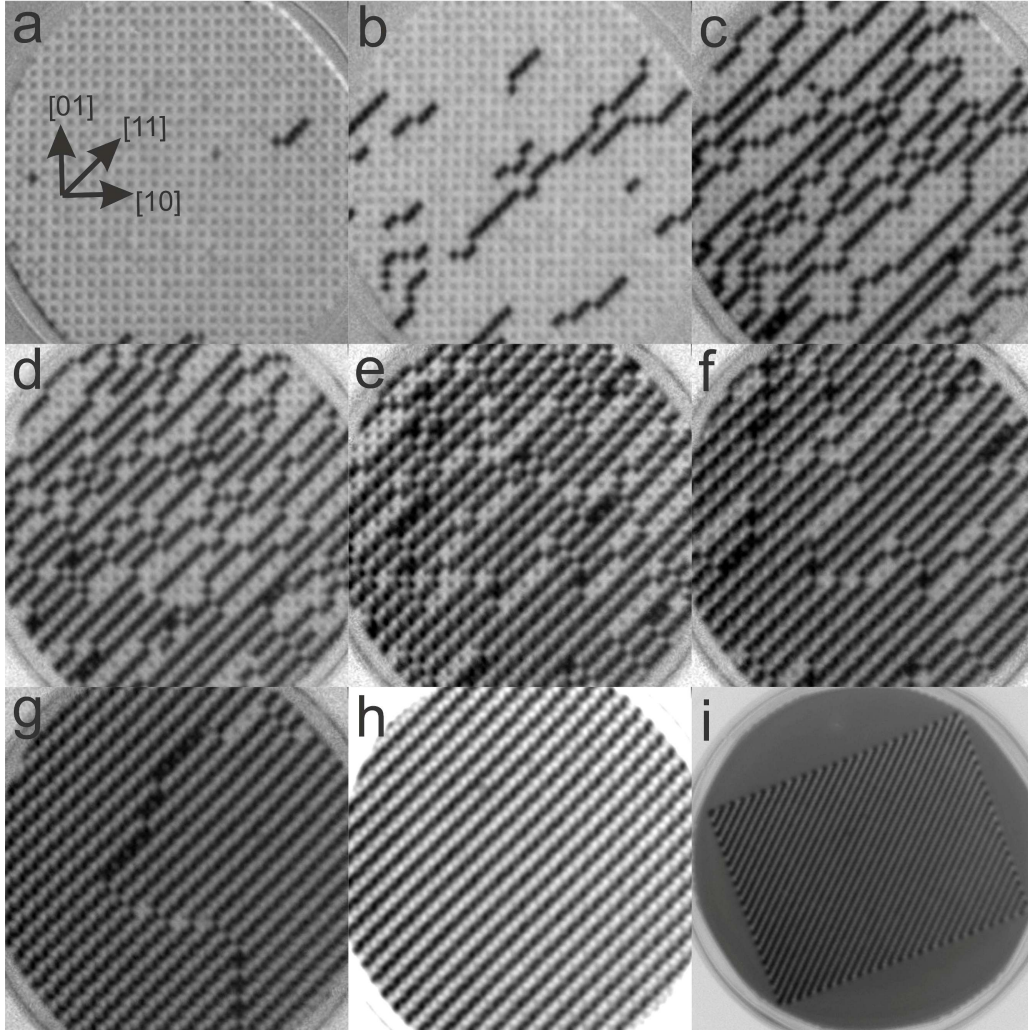


Figure 3.2: XMCD images demonstrating thermal relaxation of artificial spin ice. 20 μm field of view XMCD images of the system in (a)-(d) the string regime and (e)-(g) the domain regime. Following the evolution of the domains the ground state is achieved (h) with a 100% ground state ordering as revealed by observing the whole system at a 50 μm field of view (i). Figure adapted from [25].

surface energy minimization, bigger domains expand at the cost of smaller domains through domain boundary movement until a uniform single domain is reached [see Fig. 3.2h and i].

3.4 Vertex Statistics and the Role of Disorder

Having produced a dynamically evolving artificial spin ice system that we can directly investigate with PEEM, we are able to quantify the temporal evolution of the investigated system. An elegant way to do that is to look at the vertex type statistics as a function of time [see Fig. 3.4a]. Taking a closer look, we can see that the string regime is characterized by a strong increase (decrease) of Type I (Type II) vertices. In addition, the increasing number of strings in the early stages is reflected by an initial sharp increase in the number of Type III vertices. Meanwhile, the domain regime shows generally a slow change in the vertex population, interspersed with small jumps in the number of Type I (Type II) vertices, associated with a fast movement of a Type III vertex along a domain boundary. The reason for this is that the creation of a Type III vertex defect in a domain boundary consisting of Type II vertices costs energy, while, as soon as such a defect is created, it can move with virtually no energy cost [38]. This movement often occurs beyond the temporal limits of the XMCD imaging, but several observations indicate that the movement of the Type III vertices occurs via a sequential reversal of neighboring nanomagnets [see Fig. 3.3].

3.4.1 Kinetic Monte Carlo Simulations and the Role of Disorder

Within a close collaboration, Dr. Peter Derlet (Paul Scherrer Institute) provided us with the tools to perform Kinetic Monte Carlo (KMC) Simulations corresponding to the temporal evolution of thermal relaxation in our artificial square ice arrays. KMC is the ideal tool to get a deeper insight into the energetics, potential landscape and transition rates within a dynamically evolving system.

For the KMC simulations performed in our work the dipolar Hamiltonian described in Eq. 3.1 is introduced as the inter-nanomagnet interaction potential. Then, a simplified kinetic model [39] is applied, in order to stochastically evolve the moment configuration, where the moment reorientation rate of the nanomagnets is assumed to follow an Arrhenius type behavior, given by:

$$\nu = \nu_0 \exp(-E/k_B T) \quad (3.2)$$

ν_0 being an intrinsic reorientation prefactor, which can be strongly dependent on nanomagnet shape and volume [40], and E a reorientation barrier energy equal to the sum of the intrinsic barrier energy (shape anisotropy), $E_0 = K_{eff}V$, and half of the dipolar energy gain associated with the particular moment reorientation [5, 25]. For the calculation of the dipolar energy, we treat each nanomagnet as a point source, with each moment equal

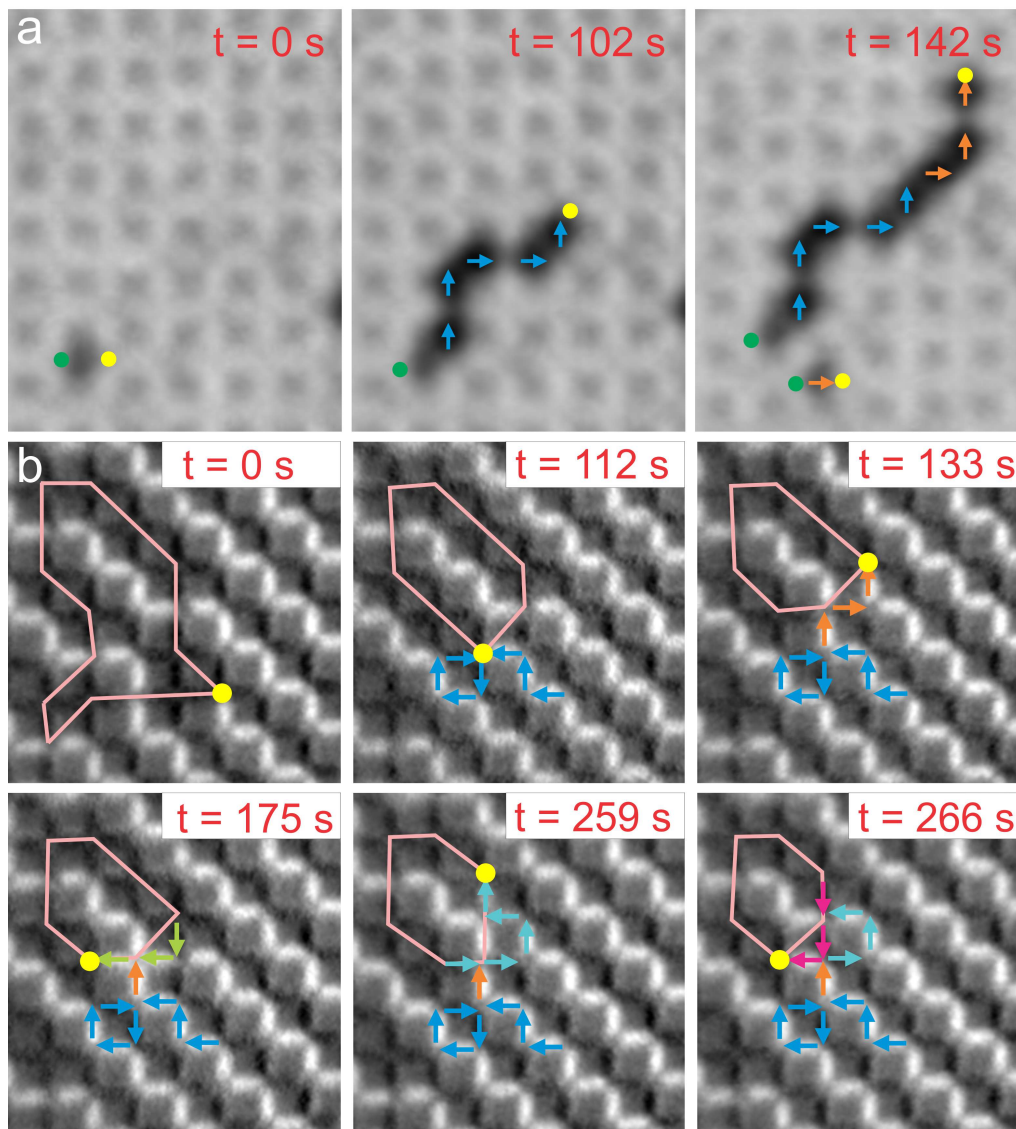


Figure 3.3: Type III vertex migration (green and yellow dots): (a) In the string regime, pairs of Type III vertices are created and separate via nearest neighbor or next-nearest neighbor moment reversal. (b) In the domain regime, a Type III vertex travels along various routes within a Type II domain boundary (pink line) so that the bigger Type I domain expands at the cost of the smaller domain. The path taken by the Type III vertex is indicated with colored arrows. Figure adapted from [25].

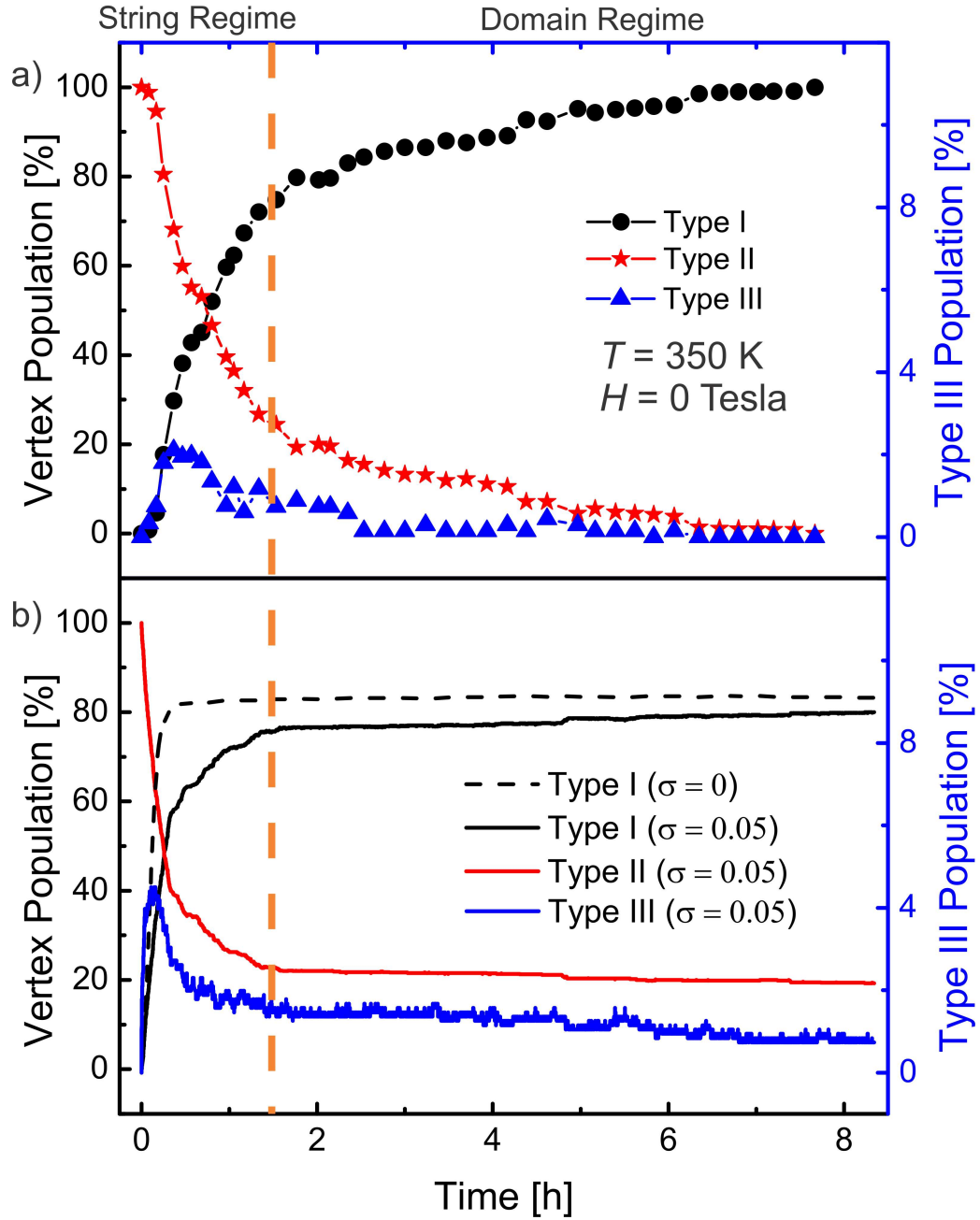


Figure 3.4: Vertex type population as a function of time. (a) Experimental data obtained at a constant temperature of 350 K, showing a 100% ground state ordering within 8 hours. (b) Kinetic Monte Carlo simulation data for a Gaussian disorder in the intrinsic nanomagnet energy barrier with a standard deviation $\sigma = 0.05$ and also for the case of no disorder, $\sigma = 0$. Figure adapted from [25].

to the product of the nanomagnet's magnetization, M , and the experimental nanomagnet volume. While we considered contributions of up to the sixth nearest neighbor nanomagnet, we found out that taking only the nearest and next-nearest neighbor contribution into account was enough for good agreement with the experiment. The addition of further nanomagnet contribution did not result in any clear improvement in agreement [25].

For reasonable agreement to experiment, values of shape anisotropy $E_0 = 1.05$ eV, saturation magnetization $M = 350$ kA/m and attempt frequency $\nu_0 = 0.5 \times 10^{-12}$ s $^{-1}$ were used in the Kinetic Monte Carlo simulations. It was also found that a certain degree of disorder (variation in the nanomagnet anisotropy energy) was required in the Kinetic Monte Carlo model to better reproduce the experimental observations of the increase in Type I vertex population at the start of the string regime [see Fig. 3.4]. We used a similar approach to that taken by Budrikis *et al* [38]. This was achieved by randomly varying the intrinsic energy barrier of each nanomagnet using a Gaussian distribution centered on E_0 with a standard deviation of $\sigma = 0.05$ eV [25]. Disorder leads to a shift in the potential energy landscape, thus allowing the system to explore a variation of different pathways towards the ground state [38, 41]. A characteristic feature of a system with intrinsic disorder is the stepped structure in the temporal evolution of the Type I and Type II vertices. As a consequence, systems incorporating disorder require much more time to reach the 100% Type I vertex configuration, than systems with no disorder [25] [see Fig. 3.4b].

3.5 Excitations out of the ground state

For both experiment and simulation, the early stages of the string regime are characterized by the creation of isolated pairs of neighboring Type III vertices [see Fig. 3.3a]. This is followed by further moment reorientations resulting in a rapid separation of the Type III vertex pairs associated with the expansion of a chain of Type I vertices between them along the [11] direction. This can be understood by considering the change in the dipolar interaction energy, following configurational changes out of an initially fully saturated (100% Type II background), which is shown in Fig. 3.5 (orange circles and continuous line). Out of a Type II background, the creation of a Type III vertex defect pair is associated with a small energy cost (less than 0.1 eV). As soon such a vertex defect pair is created, the interaction energy seems to have a negative slope with an increasing separation of the Type III vertices. In other words, Type III vertex pairs created out of a Type II background will repel each other [25, 42].

Following thermally induced magnetic relaxation, going through the aforementioned string and domain regime, an artificial square ice array will end up in one of the two degenerate ground state configurations (100% Type I) [see Fig. 3.2h and i]. As soon as the ground state is achieved, seemingly no further configurational changes occur, at least within the time scale of XMCD imaging (7-9 seconds per image). Again, this can be understood

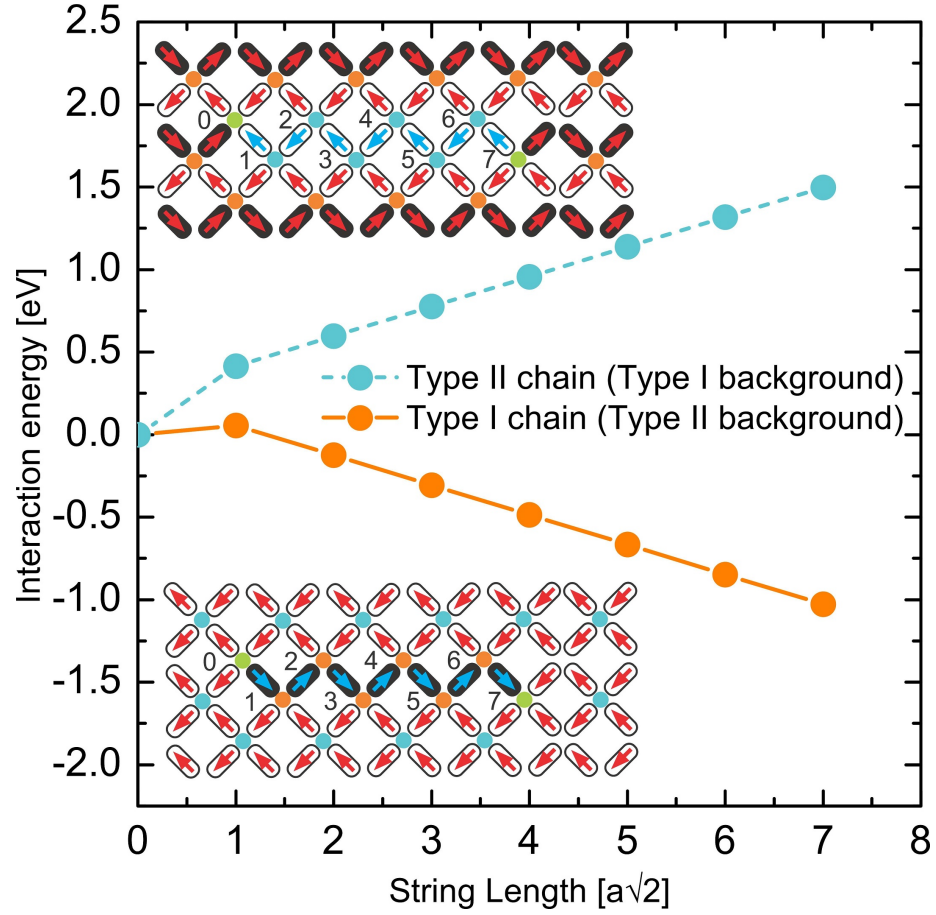


Figure 3.5: Interaction energy as a function of string length connecting two isolated Type III vertices. Type I and II vertices are indicated by orange and blue dots, respectively, and the numbers in the schematics indicate the string length as the right-hand Type III vertex follows a zig-zag path. Figure adapted from [25].

by looking at the interaction energy as a function of Type III vertex separation length within a given background, in this case a Type I (ground state) background [see Fig. 3.5 blue circles and dotted line]. The creation of a pair of Type III vertex defects out of a Type I vertex background requires a significant amount of thermal energy. The energy Barrier, E , in Eqn. 3.2 will then be roughly around $(E_0 + \Delta E/2) = 1.5$ eV, thus, any excitations created within the ground state background will have a short life time, of the order of a few hundred milliseconds, thus much faster than the time scale of usual XMCD imaging.

Towards the end of the PhD project, we performed some preliminary PEEM measurements using a single-polarization imaging mode (see experimental methods). This would theoretically allow us to observe configurational changes at a time scale of 500-700 ms, but issues with the image quality [see Fig. 3.6] over a large field of view at such short time illumination times sustained and meant that a reliable analysis was not possible to be made. Scattering techniques, which just recently emerged [43], might allow the dynamics of artificial spin ice to be investigated at much shorter time scales.

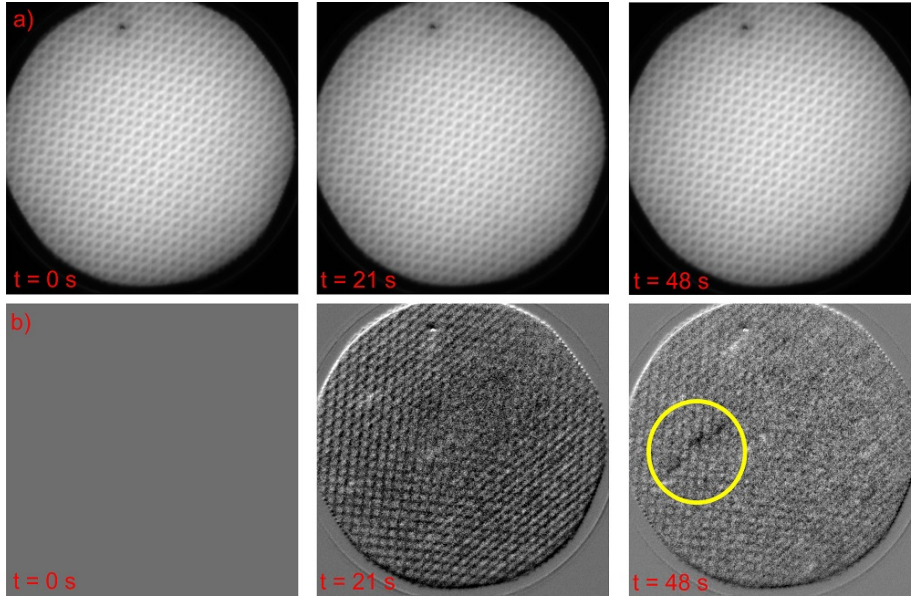


Figure 3.6: Excitations out of a Type I (ground state) background. (a) Single polarization images obtained with an exposure time of 700 ms. Images were obtained at room temperature. (b) Difference images, where the first image of a sequence is subtracted from the rest of the sequence, thus revealing eventual configurational changes as a function of time. The yellow circle highlights a region where a string of reversed nanomagnet moments (dark contrast) appears.

3.6 Conclusions

By patterning a permalloy wedge film, we were able to create artificial square ice structure with a variation in energy barriers for thermal fluctuations. By obtaining XMCD images with photoemission electron microscopy (PEEM), we were able to directly observe thermal relaxation processes occurring in artificial square ice, going from an energetically excited state down to one of the two degenerate ground states. In the experiment, we see that as soon the system falls into a single ground state domain consisting only of Type I vertices, no further configurational changes are observed. This is an example of the confining potential associated with the Type III vertices occurring in two dimensional artificial square ice systems that dominates over the negligible Coulomb interaction between charged vertex pairs [25, 42, 50].

Parallel to our work, other research groups presented alternative methods for thermal annealing. Here, the artificial spin ice systems are heated above the Curie temperature of the patterned material, then imaged with magnetic force microscopy (MFM) after cooling down below the Curie point [44, 45]. While similar effectiveness in the achievement of long-range ground state ordering was observed, these methods lack the possibility to directly observe the ordering mechanism in real space and time as we have done [see Fig. 3.2 and Fig. 3.3]. Alternatively, a different route has been pursued, that involved patterning ultrathin δ -doped Pd(Fe) layers [46, 47] with artificial spin ice structures. Here a "melting" of an initially saturated and fully ordered state was observed upon heating towards the Curie temperature [48]. While this method does provide a potential to perform annealing experiments on artificial spin ice structures, the inter-nanomagnet dipolar coupling proved to be too low to achieve high percentages of low-energy configurations [49].

By a direct comparison of experimental observations with Kinetic Monte Carlo simulations, we were able to derive several system parameters such as disorder, which is reflected by a variation of the nanomagnet's energy barriers (shape anisotropies) for thermal fluctuations.

Chapter 4

Building blocks of artificial kagome spin ice

In the upcoming two chapters, we aim to discuss the results obtained in investigating thermally activated artificial kagome spin ice, which in contrast to artificial square ice, is highly frustrated and far more complex in its behaviour. Due to the expected complexity of the system, we preferred to use a bottom-up approach in our investigation, by looking at the so-called building block structures of artificial kagome spin ice [10, 5, 51], thus, going from one-ring up to seven-ring structures. These building blocks of artificial kagome spin ice are the main focus of the current chapter. The results and text presented in this chapter are mainly taken from our recent publications [5, 51].

4.1 State of the Art

Up to the point when this PhD project started, most artificial spin ice systems were patterned from permalloy or cobalt films with thicknesses ranging between 20 and 30 nm. As permalloy has negligible magneto-crystalline anisotropy, the energy barrier to thermal fluctuations of the magnetic moments is proportional to the shape anisotropy and the volume of the nanomagnets ($E_B = K_{eff}V$). Thus, such nanomagnets possess anisotropy energies that require temperatures of the order of 10^4 K to allow for thermally driven moment reorientations at experimentally accessible time scales. Most experiments to date were therefore focused on field driven processes, either consisting of demagnetizing protocols that involved rotating a sample in a decreasing magnetic field in order to achieve low-energy states [6, 9, 10] or magnetization reversal experiments with observations of emergent magnetic monopoles [12, 13].

In order to achieve an improved analogue to the bulk spin ice, one of the key goals in the field has been to realize and investigate thermally active artificial spin ice. Morgan et al. [8] observed that a long-range ordered state can be accessed in an as-grown artificial square

ice, indicating that the ordering process occurs during the early stages of film deposition. This suggests the possibility to obtain a thermally active artificial spin ice in ultra-thin films and in recent work on patterned ultra-thin Fe films [48], it was shown how remnant configurations of artificial square ice, which are frozen at low temperatures, started to "melt" with increasing temperature via thermally induced moment reorientations in the nanomagnets. It was also recently shown that long-range ordered low-energy states can be achieved via thermal annealing [25, 44, 45]. Finally, time-resolved real space observations revealed both thermally activated moment reorientations and magnetic ordering in building blocks of artificial kagome spin ice of up to three rings [5] and extended arrays of artificial square ice [25].

4.2 Geometry, Energy spectra and low-energy states

As mentioned in the previous chapter, artificial square ice exhibits a non-equal dipolar interaction between the four nanomagnets meeting at each vertex, and therefore possesses an energy landscape where the ground state configuration is clearly separated from the rest of energy levels, making it possible to achieve a long range ordered ground state configuration in artificial square ice via thermally driven moment reorientations of the nanomagnets [25].

In contrast to artificial square ice, the dipolar interactions between the nanomagnets meeting at a vertex in artificial kagome spin ice are all equal. Artificial kagome spin ice is therefore highly frustrated, with the so-called ice-rule [26] involving either two moments pointing towards and one moment pointing out of the vertex where three nanomagnets meet (two-in/one-out) or vice-versa (one-in/two-out) [see Fig. 4.1a]. We investigate the possibility to achieve low-energy states via thermal annealing, and in particular, we aim to determine the percentages of *lowest energy* (ground) states achieved [51].

By calculating the dipolar energy of all possible moment configurations, a spectrum of states is revealed for each finite kagome structure. The spectrum is organized into bands separated by energy gaps, with the low energy states occupying the first (lowest) band. For one-, two- and three-ring structures the first band consists of 2, 6 and 24 low energy states, respectively [10, 5, 51]. Within the first band each finite system will have a particular set of absolute lowest energy states (ground states) [see Figs. 4.1b-f]. Ground state configurations are characterized by a maximization in the number of rings in the vortex state [53, 54, 10] i.e. all nanomagnet moments pointing in same sense around a ring, which corresponds to the smallest closed loop, either clockwise or anticlockwise [53, 54, 10]. Besides these ground states, there is a certain number of additional low energy states in the first band. For two- and three-ring structures, the so-called external flux closure states, where perimeter nanomagnets have all of their moments pointing head-to-tail [Figs. 4.1b-f], are the only other low energy configurations. For structures with four rings or more, further types of configurations belong to the first band [see Figs. 4.1e-f]. In the second band, the

three-nanomagnet (frustrated) vertices still obey the ice rule, but there are a number of head-to-head and tail-to-tail moment alignments appearing along the perimeter at two-nanomagnet (unfrustrated) vertices. For the case of one-, two- and three ring structures, the second band consists of 24, 32 and 179 configurations, respectively [10].

In contrast to the dipolar energy calculations performed for artificial square ice [25] (chapter 3) and previously reported work on artificial kagome spin ice [13], where each nanomagnet is replaced by a point-like dipole, our experimental results (see following sections) in thermally active artificial Kagome spin ice required us to adapt a more realistic model, that takes the spatial extent of the nanomagnets into account. The basic principles of the applied model shall now be discussed in the following subsection.

4.2.1 Simplified Micromagnetic Model

As Permalloy has a negligible crystalline anisotropy, two fundamental interactions will mainly contribute to the total magnetic energy in a given nanomagnet; that of exchange and magnetostatic self interaction. For the very thin nanomagnets considered here (where the thickness of each island is never more than several nanometres), the exchange contribution dominates the internal relaxation, and all internal moments can be considered to be perfectly aligned. This considerably simplifies the calculation of the total magnetic energy, since the intra-island magnetostatic energy (shape anisotropy) is now minimized when the total moment of each island is aligned either parallel or anti-parallel along its axial length. The only remaining contribution is the inter-island dipolar energy, which is now the sole contribution to the energy. There are a number of methods to calculate this energy, one of which is to discretize each island into an array of sufficiently small cells such that the magnetization is uniform across a single cell. The cells then are coupled via the dipolar interaction, which now can be calculated by a double summation over the cells:

$$E_{\text{iid}} = \frac{\mu_0(\Delta V M_s)^2}{8\pi} \sum_{i,j} \frac{1}{|\mathbf{r}_{ij}|^3} [\hat{\mathbf{m}}_i \cdot \hat{\mathbf{m}}_j - \frac{3}{|\mathbf{r}_{ij}|^2} (\hat{\mathbf{m}}_i \cdot \mathbf{r}_{ij}) (\hat{\mathbf{m}}_j \cdot \mathbf{r}_{ij})] \quad (4.1)$$

Here $\hat{\mathbf{m}}_i$ is the moment vector within the i th cell and \mathbf{r}_{ij} is the distance vector between cells i and j , ΔV is the volume of each cell and M_s is the island's magnetization. Thus the dipolar energy scale is set by the constant $(\Delta V M_s)^2$, where $\Delta V M_s$ is the total moment of each cell.

While this micromagnetic procedure is able to accurately reproduce the correct inter-island energetics for a given choice of M_s and sufficiently small cell size, it rapidly becomes computationally intensive for increasing system size when all of possible kagome magnetic configurations are enumerated. Indeed, for an N -island kagome system, the number of possible magnetic configurations equals 2^N , indicating exponential growth in the number configurations with increasing system size. A compromise between accuracy and simplicity is therefore needed and our past work has found that the physically relevant energetics of the kagome (and square lattice) energy spectrum can be well reproduced by treating each island

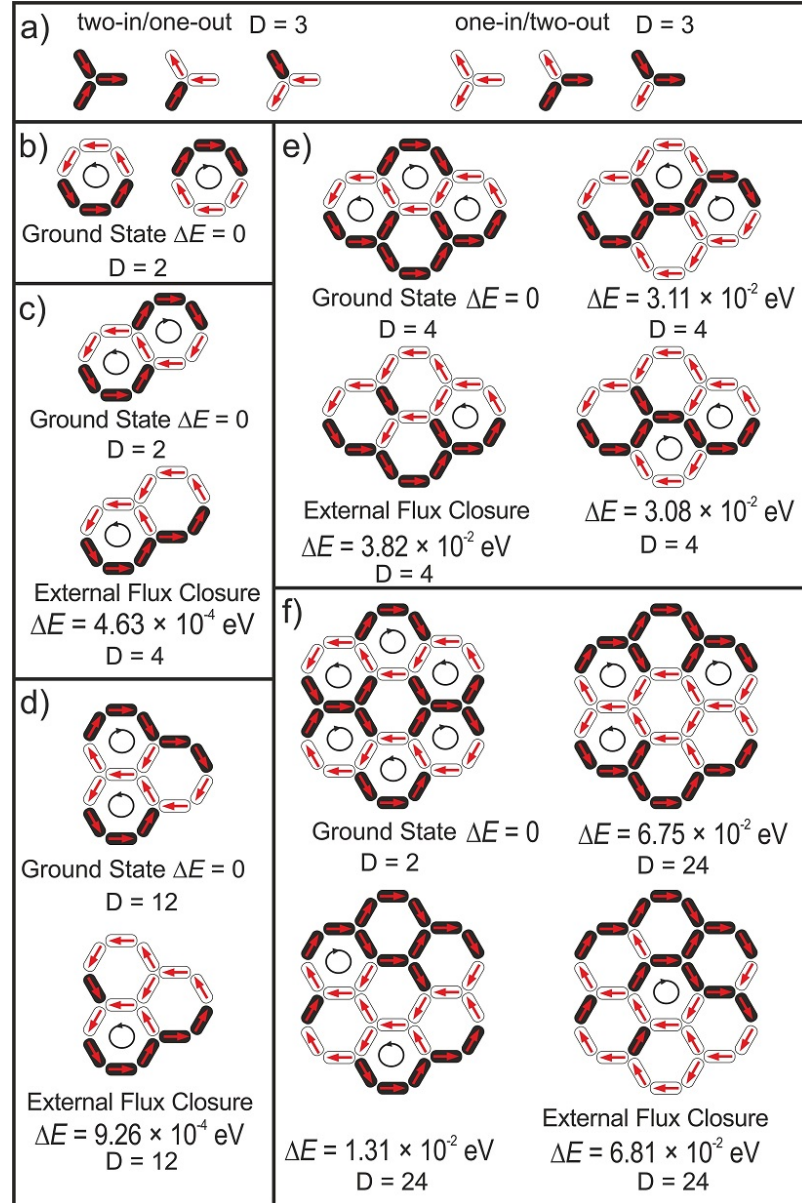


Figure 4.1: (a) The six degenerate ice-rule moment configurations at a vertex of artificial kagome spin ice. (b)-(f) Schematics of building block structures of artificial kagome spin ice and some of their low-energy states. While all shown states belong to the low-energy (first) band, all structures possess a lowest energy (ground) state, as indicated, that becomes energetically less separated from the other low-energy states with increasing system size.

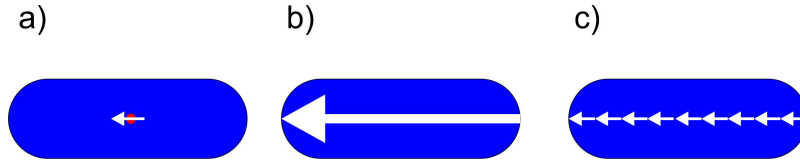


Figure 4.2: Single nanomagnet modeling. (a) Replacing a full nanomagnet with a point dipole [10]. (b) Infinitesimally thin dipolar needle, taking the nanomagnet length into account [52]. (c) Simplified micromagnetic model breaking the long dipolar needle into nine single dipoles.

as either a point dipole source [10] [see Fig. 4.2a] or an infinitesimally thin dipolar needle [52] [see Fig. 4.2b] that is discretized into a linear chain of dipolar cells [51] [see Fig. 4.2c]. This model may be seen as a simplification to the more traditional micromagnetic calculations. It should be noted that considering the width of the island was found to have little effect on the final energy spectrum [51].

For the work presented here, each island was represented as a linear chain of nine cells, each with a magnetic moment equal to $VM_s/9$ where V is the total volume of each island. To obtain the best overall agreement experiment (see section 4.3), a magnetization of 3.75×10^5 A/m was required, which is a value below that for bulk Permalloy (8×10^5 A/m), but in agreement with recently obtained values for unpatterned and patterned thin films of Permalloy [5, 25]. Figs. 4.1b-f also show the resulting energies of the finite kagome systems relative to the lowest energy state using this model.

4.3 Thickness-Dependent Ordering

Having calculated the energy spectra of the investigated building block structures, we can now investigate the possibility to achieve low-energy configurations via thermal annealing. Previously, it was found that, on application of demagnetizing field protocols [10], there is a significant decrease in the ability to achieve low energy states in the first band with increasing system size. Now, we aim to investigate the percentage of low energy states achieved by thermal activation of magnetic fluctuations and study their occupancy at room temperature following deposition, without applying external fields and without heating. In these as-grown samples, we find a strong thickness dependence on the percentage of low energy states achieved in arrays of one-, two- and three-ring structures [see Figs. 4.3b-d]. At a thickness of $d = 3.7$ nm [see Fig. 4.3b], only the strongest coupling ($a = 500$ nm) results in 100% low energy states, but at lower film thicknesses higher percentages of low energy states are achieved at all lattice parameters [see Figs. 4.3c-d]. For all structure types and all film thicknesses, reducing the dipolar coupling (going from $a = 500$ nm to $a = 700$ nm) significantly decreases the energy gap between the first and the higher energy bands, resulting in a more probable occupation of excited states, so that more states in

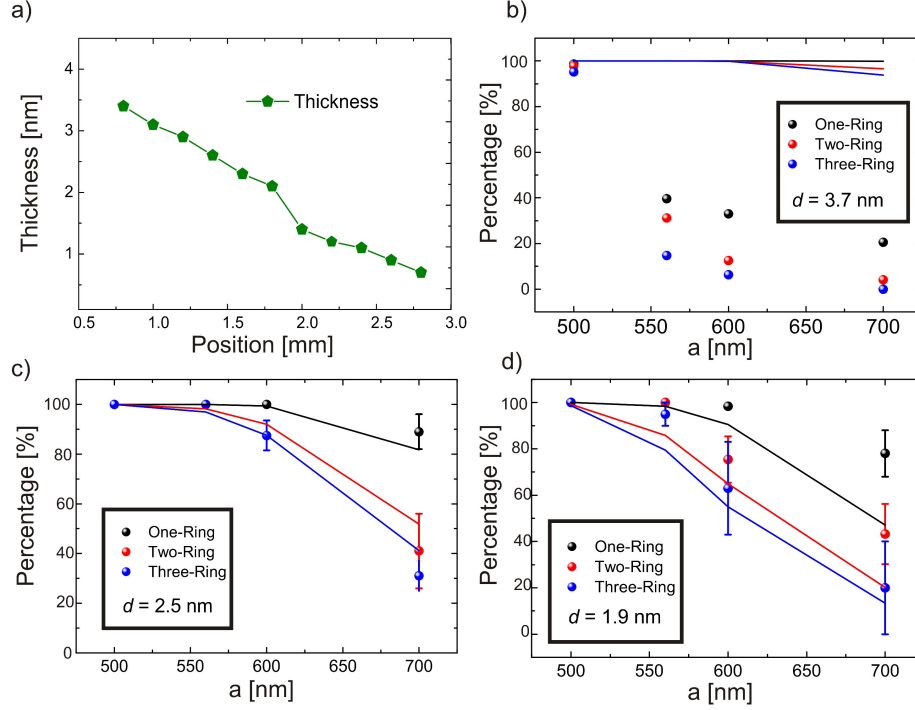


Figure 4.3: (a) Thickness of the Permalloy film measured at different positions across a wedge sample. (b)-(d) Percentages of low energy states observed at different thicknesses d as a function of the lattice parameter a ($T = 300$ K). At lower film thicknesses in (c) and (d) we observe spontaneous configurational changes within the time scale of XMCD imaging. Recording image sequences, consisting of 10 images per sequence, we determine the average percentages and standard deviations of low energy states achieved. Colored lines correspond to thermal occupancies of low energy states for one-, two- and three-ring structures derived from eqn. 4.2. The filled circles are the PEEM data and both the experimental measurements as well as the simulations were performed for lattice parameters $a = 500, 560, 600$ and 700 nm. The figure is adapted from [51].

higher energy bands are accessed. While the moment configurations are static at $d = 3.7$ nm, we start to see spontaneous configurational changes within the time scale of XMCD imaging (7-9 seconds) at lower film thicknesses (2.5 nm and 1.9 nm) [see Figs. 4.3c and d]. Here we record image sequences consisting of 10 images per sequence (80-90 seconds of observation), and determine the average percentages of low energy states achieved with the standard deviations as shown in Figs. 4.3c and d.

The strong dependence on film thickness of the experimental percentages of low energy states [see Figs. 4.3b-d] suggests a strong connection between film thickness and the timescale of the magnetic relaxation. This may be rationalized by assuming that the relaxation timescale of a nanomagnet moment will follow an Arrhenius-type behavior [25, 5] whose activation energy is given by the shape anisotropy, which itself is proportional to nanomagnet's volume. Because of this, small changes in film thickness are expected to lead to very significant changes in relaxation time scales and therefore excited state configurations as seen in figs. 4.3b-d.

To gain quantitative insight into the results of Fig. 4.3 we consider the scenario where the relaxation time-scale is well within the experimental time-scale, thus allowing the system to achieve thermal equilibrium. In this regime, equilibrium statistical mechanics can be used to calculate the average thermal occupancy of the lowest band of kagome energies:

$$\langle O \rangle = \frac{\sum_{n \in \text{first band states}} \exp\left(-\frac{\Delta E_n}{k_b T}\right)}{\sum_{n \in \text{all states}} \exp\left(-\frac{\Delta E_n}{k_b T}\right)}, \quad (4.2)$$

where n indexes each magnetic configuration and $\Delta E_n = E_n - E_0$ in which E_0 is the lowest energy magnetic configuration and E_n is the energy of the n th configuration obtained from the modelling method described in section 4.2.1.

The corresponding calculated occupancies for the three considered island thicknesses are displayed as lines in Figs. 4.3b-d. While reasonable agreement is seen for the 2.5 nm and 1.9 nm island thicknesses, there is very poor agreement for the kagome systems with an island thickness of 3.7 nm. This result may be understood by the fact that for the 3.7 nm thick structures, the relaxation time is expected to be much larger than the timescale over which the experiment was performed, and thus the observed as-grown states are generally out of equilibrium at 300 K for all but the smallest lattice constant. Indeed, the very rapid drop in occupancy with increasing lattice constant seen in Fig. 4.3b reflects that, with decreasing dipolar coupling, the kagome building block structures find it more and more difficult to distinguish the particular pathways leading to the lowest energy states. Thus the statistics seen in Fig. 4.3b originate from quenched disorder and therefore are very dependent on the thermal history and sample production method. In contrast, for the nanomagnets with a thickness of 1.9 and 2.5 nm (Figs. 4.3c-d), the magnetization dynamics are within the experimental timescale, and the system has time to fully relax resulting in annealed (thermal) disorder and hence agreement with the predictions of Eqn. 4.2. Generally, these results on as-grown building block structures confirm the importance of strong dipolar

coupling between the nanomagnets in order to achieve higher percentages of low-energy states, similar to what has been reported on as-grown artificial square ice arrays [8].

4.4 Thermally Induced Magnetic Relaxation

In addition to the possibility of achieving low-energy states, a key goal of this project was to directly observe and investigate relaxation processes in these two-dimensional artificial frustrated systems. Having a patterned Permalloy wedge film allows us to vary the energy barrier for thermal fluctuations and transition rates. Ideally, these transition rates match the temporal resolution of XMCD imaging (7-9 seconds), allowing us to directly observe thermally induced magnetic relaxation in building block structures of artificial kagome spin ice [5, 51].

The applied annealing protocol can be broken down into two major steps: The first step is performed below the nanomagnet blocking temperature ($T_B = 320$ K) and involves the application of a magnetic field (35 mT), so that all moments are set to point towards the direction of the applied field. Thus, the magnetic configurations are initially in well-defined high-energy states. As a second step, the sample is heated slightly above the blocking temperature and spatially resolved real-time observations of thermal relaxation of the artificial kagome spin ice structures are carried out. In order to avoid possible sample damage that can occur as a result of strong heating, the experiments are performed close to room temperature. The ideal film thickness then has to be determined for which the moments are static at room temperature and some heating (up to 320-330 K) is required in order to observe configurational changes within the temporal resolution of XMCD imaging. A film thickness of apprx. 3 nm was found to be ideal for this purpose. Initially, the energy barrier is high enough to prevent a spontaneous relaxation at room temperature within the timescale of a single measurement. By heating up to 330 K, we can observe how kagome building block structures relax towards the first energy band via thermally activated moment re-orientations 4.4.

This is demonstrated for a strongly-coupled three-ring structure ($a = 500$ nm) in Figs. 4.4a-h. Following the application of a saturating magnetic field, the configuration is in an energetically higher state, which belongs to the second energy band. With the onset of thermally induced moment reorientations on heating, we observe spontaneous configurational changes between the high-energy states with similar energies within the second band [see Figs. 4.4a-e] during approximately two minutes. Eventually, the reversal of the inner horizontal nanomagnet moment, together with two nearest-neighbor reversals, leads to the formation of two rings in clockwise and anticlockwise vortex states, and a reduced dipolar energy [see Figs. 4.4f-g]. From this state, the system is only one moment flip away from the first energy band and roughly three minutes after the start of the experiment, the first band is reached [see Fig. 4.4h].

Applying the same method of saturating and heating of one-, two- and four-ring struc-

tures revealed similar relaxation processes, always starting with the higher energy states and relaxing to the low energy states in the first band. In order to determine the percentages of low energy states after relaxation (after approximately one hour), we cool the system down to room temperature, so that the observed low energy states are frozen and can be counted. Up to a lattice parameter $a = 600$ nm, we see 90-100% low energy states achieved for all kagome building block structures [see Fig. 4.4i]. This demonstrates the high efficiency of thermal annealing for obtaining low energy states compared to field-driven demagnetizing procedures, where an increasing system size leads to a significant decrease in the percentage of low energy states achieved [10]. The percentages of low energy states achieved following field demagnetization [10] are shown in Fig. 4.4i for comparison. With increasing lattice parameter (decreasing dipolar coupling), there is a decrease in the percentage of low energy states from 90-100% at $a = 600$ nm to only 16% for single-ring structures at $a = 800$ nm [see Fig. 4.4i], demonstrating the important role of dipolar coupling between the nanomagnets for achieving the low energy states.

4.5 Hyper-cubic Energy Landscapes

Being able to directly observe thermally driven dynamics in artificial spin ice structures, we are able to visualize configurational changes as a function of time. A deeper insight into the thermal behavior is gained by an understanding of the underlying potential energy landscape, where its valleys (metastable magnetic configurations) control the thermodynamics and its ridges (barrier energies) control the timescale at which phase space is explored.

For the case of single-ring Kagome structure, consisting of six dipolar coupled nanomagnets, the potential-energy landscape has $2^6 = 64$ energy minima (magnetic configurations), all of which can be represented by the network graph of a 6D hyper-cube [Fig. 4.5, left panel]. Such network graphs and their corresponding theory can provide quantitative insight into the connectivity of complex systems. For example, network theory has been used to determine optimal athermal field-cooling protocols to access the low-energy configurations of thermally inactive bulk artificial spin-ice systems [41]. In the frame of the current work, network graphs are used as a visual guide to gain explicit insight into the low-energy sector of the finite kagome system potential-energy landscape. In such a graph, each vertex represents a magnetic configuration and each edge, connecting two vertices, represents a transition path connecting two magnetic configurations through a single-island reorientation. By the coloring the vertices according to the dipolar energy of the accessed configuration, these network graphs give useful insight into the connectivity of the minima within the potential energy landscape. In practice, only transitions between low-energy states need to be considered, leading to a marked simplification of these coloured network graphs. Indeed, when considering only the low-energy sector of the landscape [Fig. 4.5, right panel], the six possible states that minimize the Zeeman energy (two of which are labelled B1 and B2) and the two lowest-energy states (A1 and A2) become clearly evident,

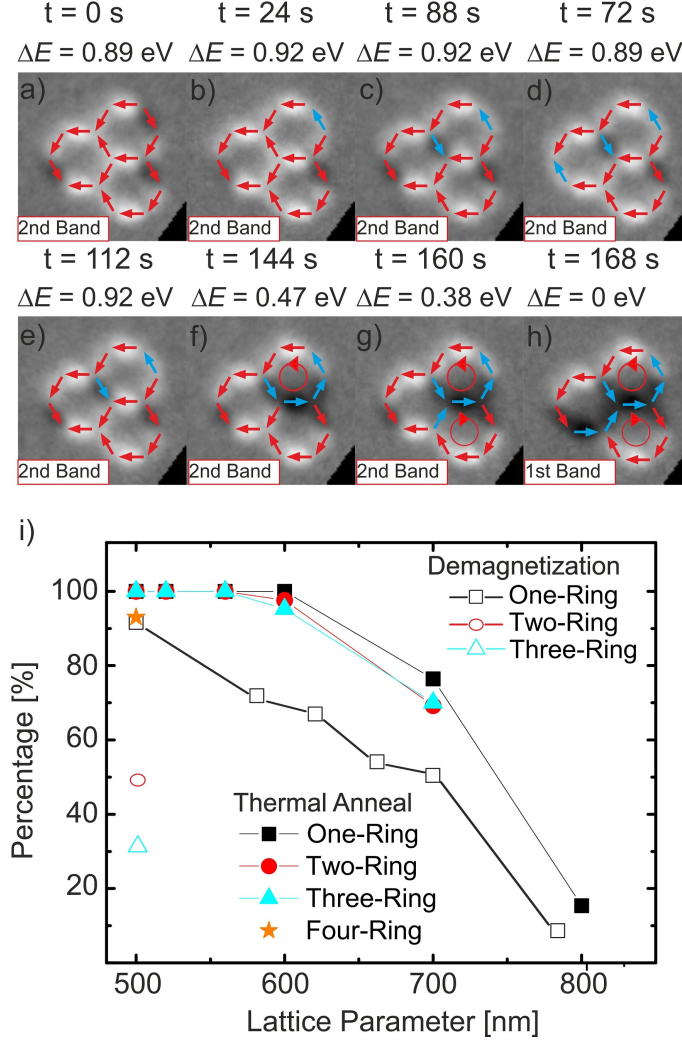


Figure 4.4: (a)-(h) Thermal relaxation of a three-ring structure ($a = 500$ nm and $T = 330$ K), going from an energetically higher state to one of 24 degenerate low energy states within 168 seconds. Blue arrows in (a) to (h) represent reversed nanomagnet moments, compared to the initial moment configuration in (a). The time t and the relative energy ΔE are shown to visualize the evolution of the system within the energy landscape (i) Percentages of low energy states achieved in arrays of kagome building blocks after thermal annealing (heating up to 330 K and cooling down to 300 K following relaxation). While the number of rings (up to three) does not seem to have a large effect on the numbers of low energy states achieved, an increasing lattice parameter (decreasing dipolar coupling) significantly affects the occupancy of the lowest energy states, which can be explained by a strong decrease in the energy gap between the first energy band and the second energy band with decreasing dipolar coupling. The percentages of low energy states achieved following a demagnetizing protocol [10] are given for comparison (open squares, circles and triangles). The Figure is taken from [51].

as do the possible paths through the low-energy states connecting A1 and A2 with B1 and B2.

Going now to two- and three-ring structures incorporating 11 and 15 dipolar coupled nanomagnets, respectively, the number of possible magnetic configurations is now 2^{11} and 2^{15} . The corresponding potential energy landscapes can be represented by 11D and 15D hyper cubes [Fig. 4.5b,c, left panel], resulting in a considerable increase in system complexity. This increase in complexity is also reflected in the increased number of lowest-energy states, which are now 6 for two rings and 24 for three rings. On increasing the number of rings, the connectivity between these lowest energy states also fundamentally changes, with a reduction in the number of low-energy paths connecting the lowest energy states and an appearance of lowest-energy states that are directly connected to each other through a single-island moment reorientation [Fig. 4.5b,c, right panel]. The reduction in the number of low-energy paths may be understood by the loss of six-fold rotational symmetry in going to two and three rings, whereas for the single ring there exist six equivalent initial transitions through which each lowest-energy state can be exited, eventually resulting in 6×2^4 direct paths linking the two lowest-energy states [Fig. 4.5a, right panel]. For the two- and three-ring kagome systems, which do not have this symmetry, the number of direct paths significantly reduces to a value that depends on the initial lowest-energy state being considered. The low-energy sector network graphs [Fig. 4.5b,c, right panel] reveal this number to range typically between 1 and 6. The clustering of the lowest-energy states seen in the low-energy sector network graphs of the two- and three-ring systems is a direct result of an increasing frustration, which increases together with the number of internal “frustrated” nanomagnets [5, 51].

4.6 Correlated Nanomagnet Activity

In the previous chapter we demonstrated the effectiveness of applied thermal annealing, in order to achieve low-energy states in building block structures of artificial kagome spin ice, especially with strong dipolar coupling between the nanomagnets. An interesting aspect of the relaxation process is that as soon the investigated structures relax to the first energy band, thermally driven moment reorientation will make them continue wandering between the low-energy states belonging to this band. Focusing on a strongly coupled single-ring structure, we can see the single-ring system reorients in a globally collective manner between the two lowest-energy configurations, upon heating to 420 K. Fig. 4.6a, left panel, shows the transitions between the clockwise and the anticlockwise lowest-energy states as time progresses. Inspection of this data reveals that within the experimental temporal resolution, such magnetic transitions are almost instantaneous and thus the intermediate states shown in Fig. 4.5a, right panel, are not resolved. By increasing the lattice parameter to 600 and 700 nm, and therefore decreasing the inter-island dipolar coupling strength, the magnetic transitions become less collective with the system spending more time in the

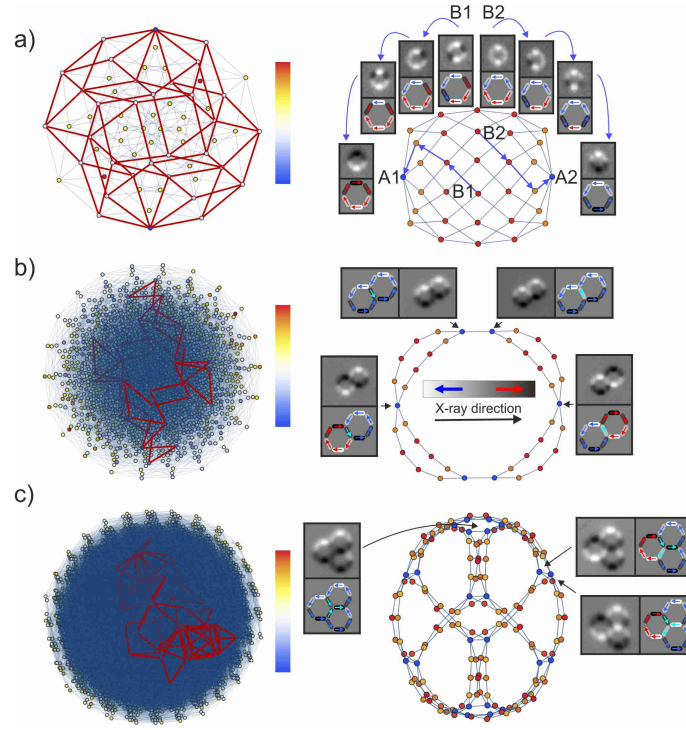


Figure 4.5: Hyper-cubic energy landscapes of finite artificial kagome spin ice systems. (a) (left panel) Network graph of a single kagome ring in which the vertices represent the $2^6=64$ possible magnetic configurations (the minima of the potential energy landscape) and the light blue edges connect one magnetic configuration to another via a change in magnetic state of a single island (the saddle points of the potential energy landscape). Each vertex is coloured according to the total dipolar energy of the corresponding configuration, given by the colour bar where blue/red indicates the lowest/highest energy. Highlighted in red is the sub-network defined by the low dipole-energy sector, which is shown as a spring electrical embedding (right panel). Here the (two) lowest energy magnetic configurations are again coloured blue. Experimentally, the system can be brought to the excited state (B) in an applied magnetic field, which subsequently decays to either of the two lowest energy states (A1 and A2) via a variety of pathways, two of which are highlighted in blue. Also shown are the corresponding experimental XMCD images taken at a temperature of 320 K of the states A1, A2, and B as well as the intermediated states of the emphasised pathways, each with a schematic showing the respective moment orientations. At a temperature of 420 K the system spends most of its time at or near one of the two lowest energy configurations, occasionally transiting to the other lowest energy state via a path that traverses the entire low-energy sector potential energy landscape. (b) (left panel) Similar network graph for the two ring kagome system showing the $2^{11}=2048$ possible magnetic configurations with the resulting low energy sector sub-network graph (right panel) connecting the now six lowest energy states (the blue vertices). The sub-network graph indicates that the low energy configurations are now either directly connected, via a local ice rule, or connected via four intermediate higher energy magnetic configurations. (c) (left panel) For the three ring kagome system, which now contains $2^{15}=32768$ vertices and a total of 24 lowest energy states, the corresponding sub-network graph (right panel) shows a clustering of directly connected lowest energy states, some of which are inter connected via four intermediate magnetic states. Thus, as the ring number increases, the connectivity of the low-energy sector dramatically changes, which has an important consequence for the nature of the magnetisation dynamics. The Figure is taken from [5].

30 intermediate excited state configurations (Fig. 4.5a, right panel) whose dipolar energies relative to the two lowest-energy states have now decreased. On further increase of the lattice parameter, island reorientation rates rise beyond the experimental time resolution, resulting in a constant zero XMCD contrast. These findings suggest that for all lattice parameters, the intrinsic individual island reorientations occur at a timescale faster than the experimental temporal resolution.

The observed dynamics can be understood using a simplified kinetic model [5], in which each nanomagnet has a characteristic reorientation rate that is modified by the change in dipolar energy between the initial and final states for the corresponding transitions, making those single-nanomagnet transitions that reduce the dipolar energy more likely. The reorientation rate will again follow an Arrhenius type behavior:

$$\tau = \tau_0 \exp \left[\frac{E_0 \pm \frac{\Delta E}{2}}{k_B T} \right] \quad (4.3)$$

with attempt time τ_0 , Boltzmann constant k_B , temperature T , and the energy difference between a magnetic moment configuration before and after a magnetization reversal ΔE . The characteristic timescale is thus set by the transition from the lowest-energy state to the first excited state of the dipolar coupled kagome system, resulting in a magnetization dynamics significantly slower than that of isolated and magnetically uncoupled nanomagnets. The simulations performed show a remarkable agreement with experiment for the single ring [Fig. 4.6a]. The unconvoluted simulation data reveal that each island occasionally reorients its moment. In most cases, such an island will return to its original magnetic state, restoring the system to its previous lowest-energy configuration. However, sometimes the moments in neighboring islands will reorient themselves before this occurs [Fig. 4.6a, right panel inset] and, in this way, the system traverses the low-energy sector of its potential-energy landscape (Fig. 4.6a, right panel). Thus, most activity involves short closed-loop pathways returning the system to its initial lowest-energy state, but sometimes a path will traverse the entire low-energy network, allowing the singlering system to attain the other lowest-energy state through a minimum of five intermediate states [Fig. 4.6a, inset, right panel]. Thus, for $R = 500$ nm, in which the dipolar coupling is the strongest, the transition rate between the two lowest-energy states is significantly less than the individual island reorientation rates, allowing the former to be experimentally resolvable as a global collective event.

For the two- and three-ring structure, it gets slightly more complicated to enumerate the different configurations. Similar to the 1-to-6 enumeration of the one-ring structure (1 stands for a clockwise orientation of all moments and 6 for an anti-clockwise orientation nanomagnet moments within a one-ring structure), we visualize the magnetic state of the system by computing the sum of the magnetic state of all islands [Fig. 4.6b, left panel]. This is achieved by assigning either a zero or one to each island, according to the convention that zero represents an anticlockwise orientation for the six islands of the first ring, the five additional islands of the second ring and the four additional islands of the third ring.

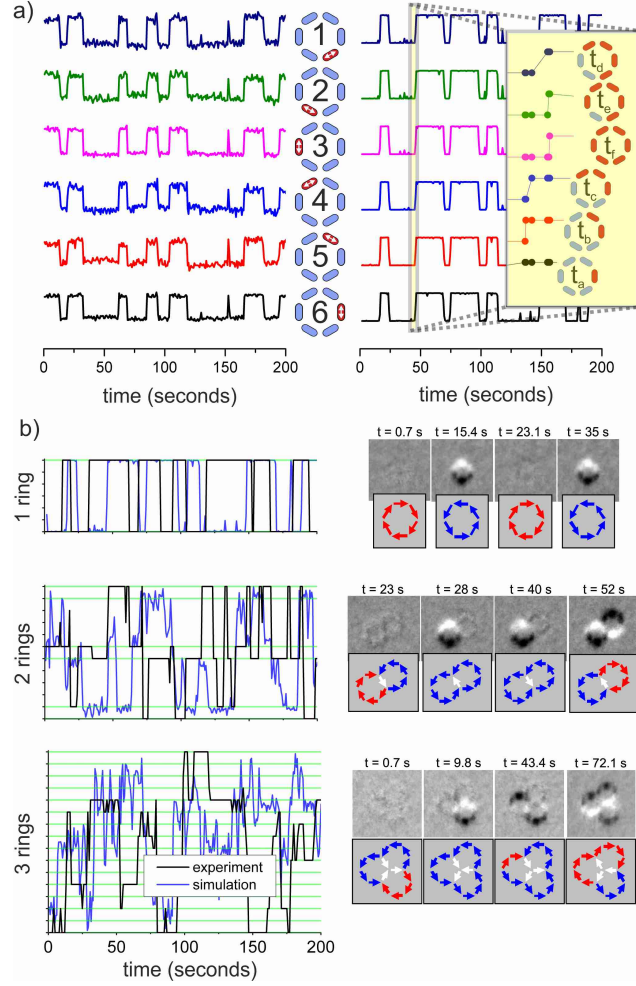


Figure 4.6: Temporally resolved dynamics of the magnetic degrees of freedom. (a) (left panel) Experimentally observed moment reorientations for each island in a single-ring system with a lattice parameter $R = 500$ nm and at a temperature of 420 K. Inspection of the magnetic states of all six islands (where the maximum values represent one moment orientation and the minimum values the other orientation) indicates a correlated switching between magnetic states with all island moments oriented clockwise and all island moments oriented anticlockwise. (right panel) Reorientation data derived from the Kinetic Monte Carlo simulations and convoluted with the experimental temporal resolution demonstrates excellent agreement with experiment. A snapshot of unconvoluted data in the highlighted region is given in the inset in which the lowest moment has first reoriented followed by the sequential reorientation of neighbouring islands until all island moments have reversed their direction and the kagome ring has entered the other of its two lowest energy states. (b) (left panel) Experimental (black curves) and convoluted simulation (blue curves) data showing the sum of instantaneous island states as a function of time for one, two and three ring kagome systems. The time spent in one particular lowest energy magnetic state (indicated by the green lines) reduces as the number of rings increases due to the changing energy landscape with not only an increase in the number of lowest energy states but also the nature of their connectivity. (right panel) Temporal sequences of the changes in magnetic state in the one, two and three ring kagome systems at 420 K, experimentally recorded as single-polarisation XMCD images. The Figure is taken from [5].

This defined quantity is plotted in Fig. 4.6b, left panel, for both the PEEM and simulated kinetic Monte Carlo data at a temperature of 420 K for all ring numbers. One trend that can be seen from Fig. 4.6b is that with increasing ring number, the system will spend an increasing time in one of the intermediate states and less time in one of the low-energy states [5].

4.7 The Effect of Increasing System Size

In the previous two sections, we already learned about the influence of increasing system size on the ordering mechanism and the exploration of the hyper-cubic energy landscape, at least for systems consisting of up to three Kagome rings. Now, we turn our focus to system sizes of four and seven rings and aim to investigate whether the predicted ground state configurations [52, 55] can be achieved, using the annealing procedure explained in Section 4.3.

As mentioned before, artificial kagome spin ice is a highly frustrated system that has a strongly increasing density of low energy states with increasing system size [10, 5]. For the case of one-ring structure, the first energy band consists of a doubly degenerate low energy vortex state [10, 5] whereas for a four-ring structure it consists of 104 low energy states. For even larger finite systems this number rapidly grows and when simulating a seven ring system, direct enumeration of the states becomes intractable and more approximate methods are needed. Here, Monte Carlo methods are used (simulations performed by Peter Derlet, PSI) to statistically sample the low energy states obtained from the modelling approach in section 4.1. This simulation was performed at $T = 1000$ K, a temperature which is sufficient to accurately probe the full spectrum of the first band plus much of the second energy band. The final density of states is obtained by multiplying the energy histogram obtained from the Monte Carlo method by the Boltzmann factor $\exp(-\Delta E/(k_b T))$ with $T = 1000$ K. The density of states for the seven-ring artificial kagome spin ice structure, in which the zero energy is taken to be the energy of the lowest energy state, is displayed in Fig. 4.7, with the two energy bands separated by an energy gap. In the upper inset in Fig. 4.7 this gap, defined as the difference between the lowest energy value of the second band and the average energy of the lowest energy states in the first band, is plotted as a function of the kagome ring number. One sees that as the structure size increases, the gap decreases and will converge to a value for very large systems that corresponds to the energy associated with locally breaking the ice rule.

For experiments at all system sizes performed at 330 K, configurations that break the ice rule or constitute a high energy excitation of the perimeter nanomagnets are never observed. For the case of the seven-ring structure, this can be understood via the lower inset in Fig. 4.7, which focuses on the first energy band and plots the Boltzmann factor at 330 K (black line), indicating the mean thermal occupancy at this temperature, and demonstrating that excitations outside the first energy band are unlikely. This also shows

that it is unlikely that the doubly degenerate ground state [see Fig. 4.1f] will be observed with the most likely states occurring at $\sim k_b T = k_b \times 330 \text{ K} = 0.03 \text{ eV}$.

By determining the percentages of *ground states* achieved for all strongly coupled ($a = 500 \text{ nm}$) structures following the annealing protocol described in section II, we confirm the increased difficulty in accessing one of the *ground states*. For one-, two-, three- and four-ring structures, the percentages of ground states observed are 100%, 32%, 62% and 13%, respectively. This is in line with the expected percentages of 100%, 33%, 50% and 4% for the same structures, taking into account the degeneracy of low energy states given in Figs. 4.1b-f. For the seven-ring structure, while there is thermal relaxation from the magnetic-field-defined high-energy state to the low energy states belonging to the first energy band, we did not observe the ground state, despite repeating the annealing procedure on several seven-ring structures and observing up to 100 different low energy states over a period of an hour. It therefore appears that lower temperatures over an extended period of time would be needed to observe the ground state in the seven-ring structure. Unfortunately, though, these temperatures are likely to be below the system's blocking temperature, resulting in a shift from probing equilibrium states (annealed disorder) to probing out-of-equilibrium states (quenched disorder).

An example of the thermal relaxation in the seven-ring structure is given in Fig. 4.8. Initially in a saturated state, the moments of the horizontal inner nanomagnets are unlikely to switch, as this would result in ice-rule violations. Therefore, non-horizontal nanomagnets reverse their moments first and initiate subsequent moment reversals while strictly maintaining the ice rule. This leads to the creation of rings with clockwise and anticlockwise vortex states or strings of reversed moments [see Figs. 4.8a-c and Figs. 4.8h-j]. In addition to vortex states, moment reversal of sequential perimeter nanomagnets leads to a low energy external flux closure state [see Figs. 4.8d-h]. Once this state is achieved, further configurational changes are dominated by moment reversals of inner nanomagnets, all locally obeying the ice rule [see Figs. 4.8i-l]. This continued exploration of the low energy sector of the energy landscape has also been reported for kagome building block structures of up to three rings [5] (see sections 4.4-5).

4.8 Conclusion

We have investigated the possibility of achieving low energy states in building blocks of artificial kagome spin ice in their as-grown state at different film thicknesses, without the application of an external field or additional heating above room temperature, and find that strong dipolar coupling is essential for achieving 100% low energy states. In addition, we performed thermal relaxation experiments, observing how the structures evolve from a high-energy magnetically saturated state to the lowest energy states for system sizes of up to seven rings. In all cases, the final states following relaxation belonged to the first energy band, which are separated by a gap from the second band. For structures

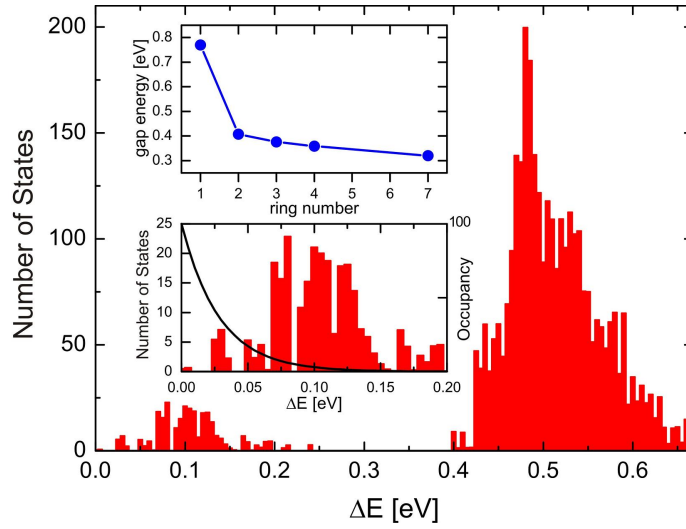


Figure 4.7: Energy spectrum calculated for a seven-ring kagome building block structure ($a = 500$ nm) revealing a gap between the first and the second energy band. The upper inset demonstrates the systematic decrease of the energy gap with increasing system size. The lower inset focuses on the first (lowest) energy band, with the black line being a plot of the Boltzmann factor at a temperature of 330 K. Multiplying the Boltzmann factor (black line) by the calculated spectrum gives the predicted occupancy density at $T = 330$ K.

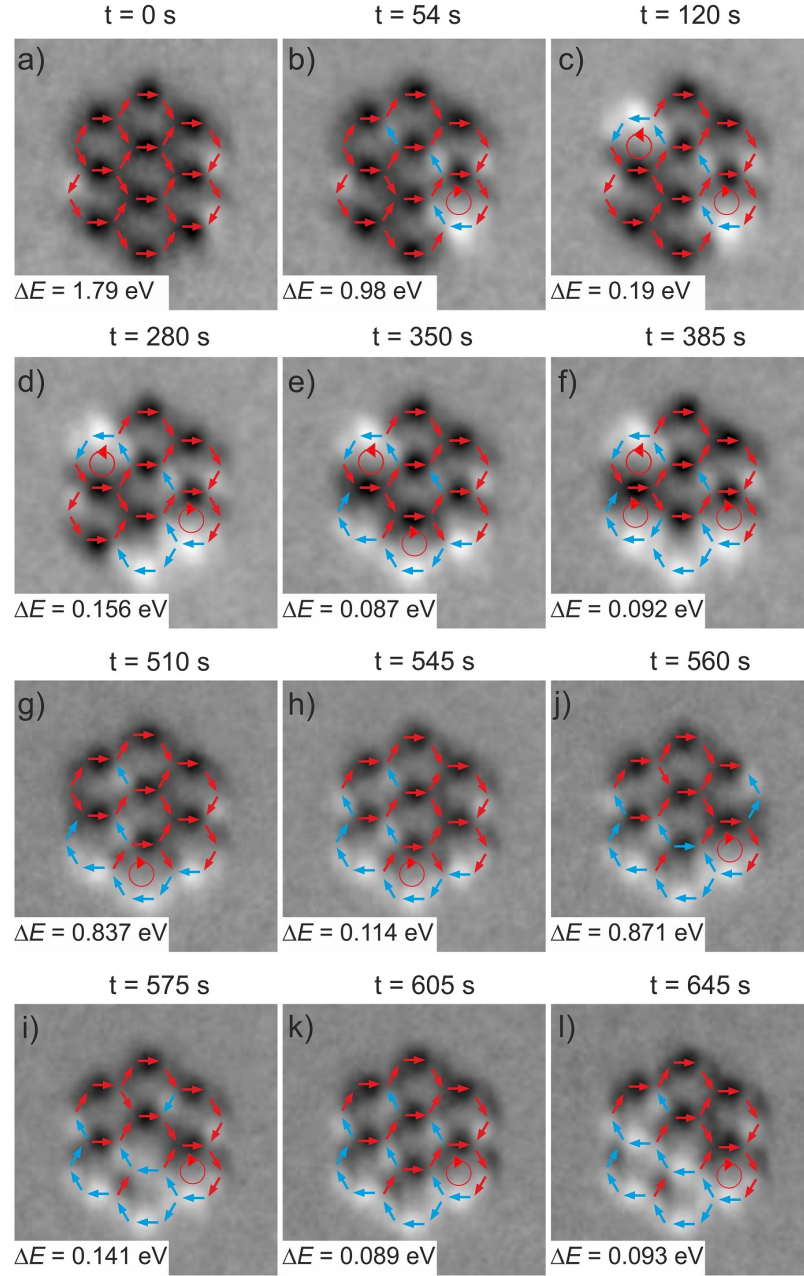


Figure 4.8: Thermal relaxation of a seven-ring artificial kagome spin ice structure ($a = 500$ nm), from a high-energy state to an external flux closure state (low energy state), where perimeter nanomagnets have all their moments aligned towards one direction (a)-(h). This is followed by a number of moment reorientations mainly in interior nanomagnets, leading to transitions between several low energy states of similar energies ΔE relative to the ground state (i)-(l). The ground state was never observed. Blue arrows in (b)-(l) represent reversed moments of nanomagnets, compared to the initial configuration in (a).

with one to four rings, we observed the ground state configurations that occur within the spectrum of low energy states. However, for the seven ring structure, thermal fluctuations allowed the system to explore the large number of low energy states without attaining the absolute lowest energy that corresponds to the long range order thought to exist in extended systems [52]. This is a direct result of the high frustration and extensive energy landscape encompassing a large number of degenerate low energy states, and is in contrast to artificial square ice, which has a distinct gap between the ground state and the next energy band, leading to a perfect order following thermal relaxation [25].

While we demonstrate in the building blocks of artificial kagome spin ice the high-efficiency of thermal annealing not seen when using demagnetizing protocols [10], extrapolating our results to extended arrays of artificial kagome spin ice, we conclude that it will be difficult to achieve the ground state [52, 55] using the presently applied thermal annealing protocol. This could have different reasons. It may, for example, be that long range ordering is not able to set in at the temperatures used in our experiments. Therefore, future work might move towards artificial kagome spin ice structures with much lower nanomagnet blocking temperatures, so that larger temperature ranges can be explored with a possibility to approach temperatures where the systems exhibit predicted phase transitions to long-range ordered ground state configurations [52, 55]. Exploring possibilities of accessing these ground state configurations will be the main topic of the upcoming chapter 5.

Other recently presented annealing procedures are based on heating above the Curie temperature and observing the frozen-in configurations with magnetic force microscopy, after cooling back to room temperature [44, 45]. In comparison, our combination of a patterned permalloy wedge and imaging with PEEM [5, 25] has the main advantage that configurational changes can be spatially resolved as a function of time. The method presented here not only delivers the possibility for direct comparison with theoretical predictions of thermal behavior [52, 55, 42, 38, 50, 56] but also the exciting prospect to directly observe and investigate the thermally driven motion of emergent magnetic monopoles in artificial kagome spin ice. In contrast to field-driven experiments [12, 13], where the magnetic monopole motion is determined by the orientation of the applied magnetic field, the thermally driven motion of emergent magnetic monopoles will be unconstrained. Future observations of this kind will provide the possibility to draw direct comparisons with the low-temperature thermodynamics of pyrochlore spin ice [57, 58, 59].

Chapter 5

Extended arrays of artificial kagome spin ice

One of the main conclusions of the previous chapter was the inability to reach the ground state configuration in artificial kagome spin ice, at least using a single cycle annealing procedure, as described in section 4.3. Now, we want to turn our focus towards extended arrays of artificial kagome [see Fig. 5.1a and b] spin ice and explore an *optimized* annealing procedure (with multiple cycling) that might lead to the formation of ground state configurations in these systems. At the time of writing this chapter, two manuscripts with associated simulations [60, 61] were still under preparation. Therefore, the chapter focuses mainly on experimental observations and the conclusions drawn should be considered as preliminary.

5.1 Introduction and Overview

Magnetic monopoles were first introduced by Dirac in order to explain the quantization of the elementary electric charge [62] and were predicted to appear in pairs of opposite magnetic charges connected by a string flux, called a Dirac string. Even though magnetic monopoles are predicted to exist in theories unifying the four fundamental laws, their direct observation remained elusive despite intensive research [63]. Recently, a new approach was introduced where each magnetic dipole is replaced by a pair of opposite magnetic charges (monopoles), in order to account for the low-temperature degeneracies in Pyrochlore spin ice compounds [7]. These emergent “magnetic monopoles” were found out to be the appropriate degrees of freedom in spin ice, to understand its low-temperature physics [64]. While the detection of these quasi-particles and their dynamics in Pyrochlore systems relied on rather macroscopic techniques such as magnetization measurements [66] or reciprocal space observations by means of diffusive neutron scattering [58], a direct real-space visualization to two-dimensional analogues has only been made possible via imaging artificial kagome

spin ice systems [12, 13].

Magnetic configurations obeying the ice rule in artificial kagome spin ice will have either two moments pointing into a vertex and one moment pointing out (or vice-versa). Configurations violating the ice rule (three-in or three-out) have a very high energy and were never observed in our experiments [5, 51, 60]. Considering the magnetic charges [64, 52] ($\pm q$), one can see that in a kagome lattice the net magnetic charge at the vertices is uncompensated. Vertices obeying the ice rule will have $\pm q$ net charge, while vertices violating the ice rule will have $\pm 3q$ net charge. Based on this model, it was predicted that the system possesses four distinct phases [52, 55]: a superparamagnetic phase, consisting of a fully disordered $\pm q$ and $\pm 3q$ (three-in or three-out vertex configurations) charge gas. Upon cooling, and with an increasing strength of dipolar interactions, the system will enter a so-called Spin Ice I phase (K1 phase), where the ice rule is obeyed at all vertices, thus creating a random distribution of $\pm q$ vertex charges. Upon further cooling, the system will enter a charge-ordered phase (K2 phase), where each negative vertex charge will be surrounded by three positive charges and each positive by three negative charges (or vice-versa) [see Fig. 5.1d]. As there are many possible moment configurations that fulfill this charge-ordering, the K2 phase is only partially ordered. Finally, a third transition is predicted, going from the charge ordered K2 phase to a phase of fully ordered moments and minimized entropy [52, 55]. Exploring possibilities to access this ground state configuration [see Fig. 4.1f] is one of the main goals of this project.

We saw in chapter 4, that achieving this ground state configuration is already not possible in seven ring structures, using a simple heating and cooling procedure. In addition, most recent investigations on thermally active artificial spin ice systems have delivered evidence for long-range ground state ordering in artificial square ice [25, 44, 45] and the formation of magnetic charge crystallites (K2 configurations) in artificial kagome spin ice [45]. However, a direct observation of the crystallization mechanism was not possible. The kagome ground state configuration remained unaccessed.

Now, using the same approach as described in chapter 3 and 4, we aim to directly observe thermal relaxation processes occurring in extended arrays of artificial kagome spin ice. Additionally, we aim to explore different annealing procedures in an attempt to access the predicted ground state [52, 55].

5.2 Thermal Relaxation and Emergent Magnetic Monopoles

Similar to the annealing procedure described in chapters 3 and 4, and focusing on a film thickness of 3.5 nm along a wedge sample, we applied a saturating magnetic field (35 mT) at room temperature ($T = 300$ K), so that all magnetic moments point towards one direction and a fully charge-ordered state of one type is created [white dots in Fig. 5.2]. Upon heating to $T = 420$ K, we started to observe moment fluctuations with a strict ice-rule obedience, which does not allow horizontal nanomagnets to reverse their moments

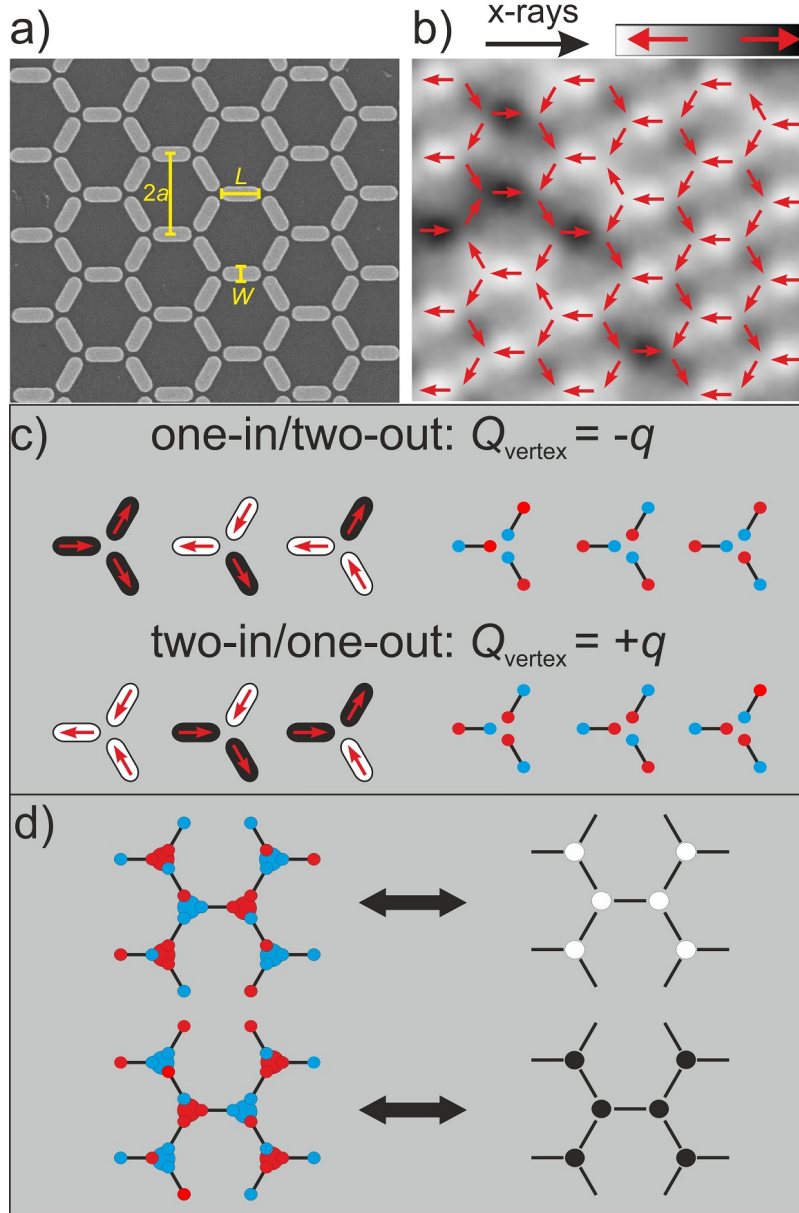


Figure 5.1: Artificial kagome spin ice. (a) SEM image of an array consisting of nano-magnets with a length $L = 470$ nm and a width $W = 170$ nm, arranged in a kagome honeycomb lattice with a lattice parameter $a = 500$ nm. (b) XMCD image revealing magnetic configurations of artificial kagome spin ice. (c) The six degenerate ice-rule moment configurations at a vertex of artificial kagome spin ice and their *magnetic charge* representation. In artificial kagome spin ice, the net magnetic charge at the vertices will be uncompensated. Vertices obeying the ice rule will have $\pm q$ net charge. (d) Two opposite types of charge-ordered configurations.

first. Instead, we at first only observed magnetization reversal of tilted nanomagnets, thus creating isolated charge defects [yellow dots in Fig. 5.2b], which are followed by next-nearest neighbor moment reversals [see Fig. 5.2c and g-i]. This leads to the creation and expansion of opposite charge-ordered domains, compared to the initial saturated state [black dots in Fig. 5.2]. While horizontal nanomagnets are initially not allowed to switch their moments, they do switch eventually to connect two tilted nanomagnets with reversed moments [see Fig. 5.2d], as this “bridge mechanism” does not violate the ice-rule. This leads to sequential separation of the charge defects, leaving charge ordered regions behind, which have the same type of charge order as in the initial state [white dots in Fig. 5.2e-f]. All mechanisms of charge defect creation and propagation, schematically shown in Fig. 5.2a-f, lead to the formation, expansion or shrinking of opposite charge ordered domains [see Fig. 5.2g-j].

Using the definition proposed in refs. [12, 13], we are able to identify that some of the observed defects correspond to emergent magnetic monopoles [64]. This is best done by looking at the so-called smeared charge density maps. These maps emerge as a convolution of a given vertex charge distribution with a Gaussian function of FWHM, $\Delta x = 2a_h$, a_h being the distance between neighboring vertices [13]. Thus, non-charge-ordered vertices will give rise to non-zero value in a smeared charge density map. Besides vertex defects, vertices residing at the edges of charge-ordered domains will also give rise to non-zero values in the smeared charge density map [see Fig. 5.3]. It seems therefore, that vertex defects, according to our definition, can be considered as emergent magnetic monopoles. Thus, similar to previous work by Mengotti et al. [13], the smeared charge density maps are the most efficient way to look for emergent magnetic monopoles and our defined defects may be used as an orientation to look for these emergent magnetic monopoles.

In contrast to field-driven experiments in artificial kagome spin ice [12, 13] and thermal relaxation observed in artificial square ice [25], our thermally active artificial kagome spin ice arrays seem to strictly obey the local ice-rule, which leads to a drastic difference to field-driven experiments. As mentioned before, we start from a fully saturated state, thus creating a fully charge-ordered configurations. Upon heating to 420 K, the thermal energy is high enough to overcome the barrier for thermal fluctuations. The strict ice rule obedience makes it unlikely for any horizontal nanomagnet to switch its moment, within the given saturated background, as this would lead to an ice rule violation. Instead, we observe an initial regime of isolated moment reversal of non-horizontal nanomagnets [see Fig. 5.3a and b, left panel]. Whenever a non-horizontal nanomagnet switches, it creates a pair of vertex defects, which, when looking to the smeared charge density map, appear as emergent magnetic monopoles [see Fig. 5.3a and b, right panel]. Now, these emergent magnetic monopoles will not sequentially separate via nearest neighbor moment reversals, due to the strict ice rule obedience. Instead, they will either annihilate by a moment reversal, back to the original configuration, or wait for next-nearest neighbor nanomagnets to switch their moments, thus creating two neighboring pairs of monopole defects. Such configurations will then allow horizontal nanomagnets to switch, which leads to an annihilation of two monopoles, while the other two separate [see Fig. 5.3c and d]. This is the aforementioned

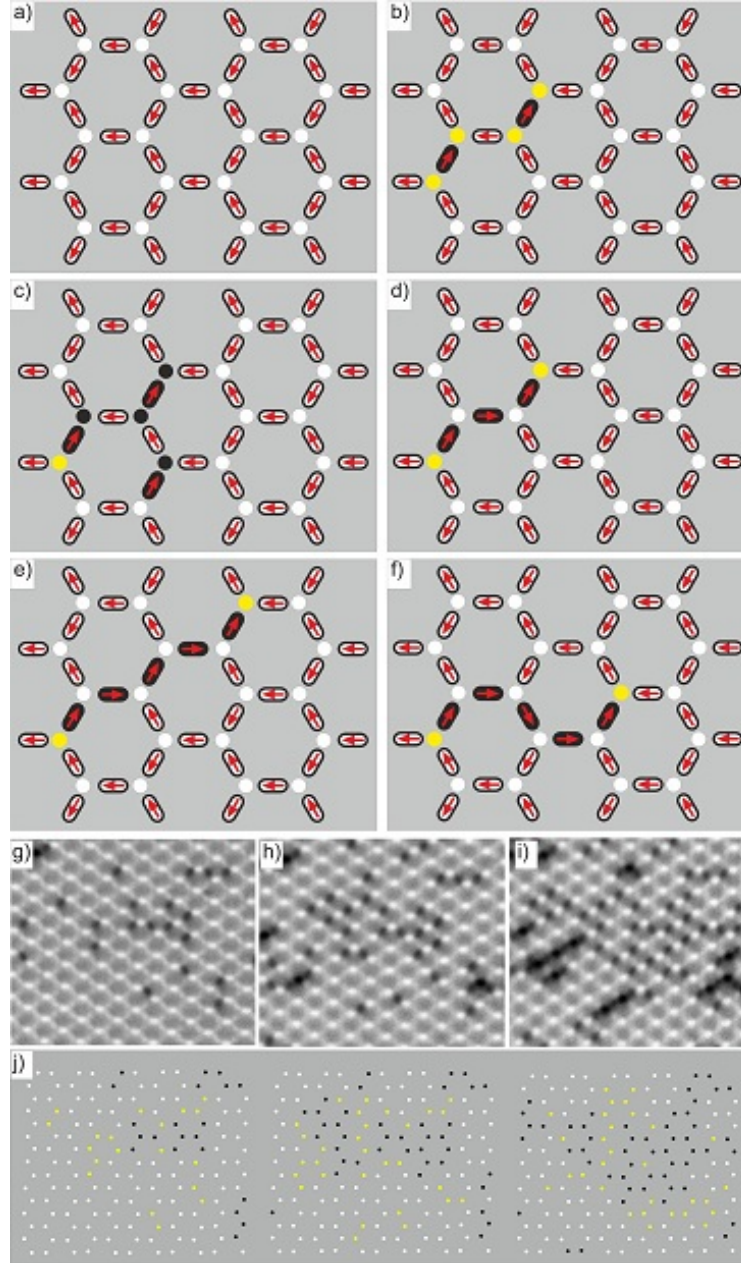


Figure 5.2: Thermal dynamics in artificial kagome spin ice. (a)-(f) Schematics of the different observed ordering mechanisms, which lead to creation and expansion of opposite charge-ordered domains. (g)-(i) XMCD image revealing magnetic configurations in thermally active artificial kagome spin ice. (j) Charge ordering, corresponding to the XMCD images in (g)-(i). Black and white dots represent the two types of charge ordered domains and yellow dots correspond to vertex charge defects not belonging to any charge ordered configuration.

bridge mechanism, which seems to be an essential part of string extension and vortex creation [see Fig. 5.3c-e]. In our upcoming publications, and in a close collaboration with Peter Derlet and Sebastian Gliga (both PSI), we aim to deliver comparisons between experimental observations and both micromagnetic and kinetic Monte Carlo Simulations [60].

5.2.1 Correlations: Quo Vadis, Ground State?

As mentioned before, the annealing protocol used thus far proved to be not efficient, in order to achieve ground state configurations in artificial kagome spin ice, already at system sizes of seven kagome rings (see Chapter 4). Nonetheless, for the sake of consistency, we applied the same protocol on extended arrays of artificial kagome spin ice and observed the thermally driven motion of emergent magnetic monopoles, but we did not manage to observe any ground state configurations in any of our long and extensive observations. As discussed in chapter 4, this might be explained by the fact that the blocking temperatures of our nanomagnets are clearly above the temperature range for observing such ground state configurations [51].

An elegant way to quantify the experimental observations is to extract inter-nanomagnet correlation values [9, 30]. Two nanomagnets at sites i and j will have a correlation value C_{ij} of +1, if the scalar product of their magnetic moments m_i and m_j is positive, and -1 , if the scalar product is negative. For a given configuration, we then calculate the average correlations for up to the third nearest neighbor [see Fig. 5.4a]. A similar definition is introduced for charge-charge correlations [see Fig. 5.4b and inset in Fig. 5.4a], where a value +1 stands for a maximization of charge-charge (coulombic) interaction and -1 for energetically unfavorable charge configurations. Correlations are measured up to the third nearest neighbors. Both the moment correlations and charge correlations show a rapid transition from non-equilibrium to equilibrium dynamics, which is marked by a stabilization of all correlation values within the first 70 minutes of relaxation. The low values of next-nearest neighbor moment correlations ($C_{\alpha\nu} = 0.03-0.04$ and $C_{\alpha\gamma} = -0.05$) indicate a weak correlation beyond the nearest neighbor nanomagnets, which might explain the impossibility to access the ground state configuration, which is expected to have correlation values of $C_{\alpha\nu} = 0.101$ and $C_{\alpha\gamma} = -0.118$ [9].

5.3 Towards Optimized Annealing

After all the results presented, so far, it is clear that the predicted ground state configuration of artificial kagome spin ice can not be achieved, using the applied annealing procedure. It became obvious that artificial kagome spin ice systems with clearly lower blocking temperatures have to be investigated [51]. While staying within the spatial resolution of PEEM imaging, we patterned artificial kagome spin ice arrays consisting of nanomagnets with lengths $L = 300$ nm, widths $W = 100$ nm and height $d = 2.5$ nm. This allowed us to move the blocking temperature down to 160 K. In addition to that, we patterned smaller

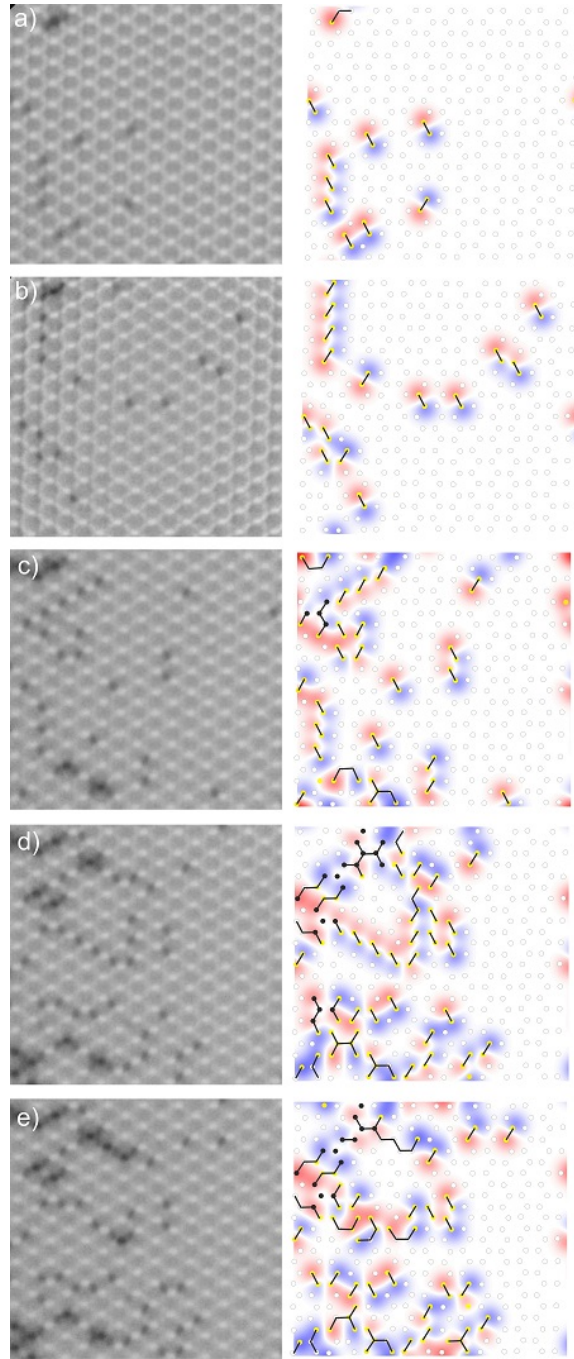


Figure 5.3: Thermally driven motion of defects and emergent magnetic monopoles in artificial kagome spin ice.

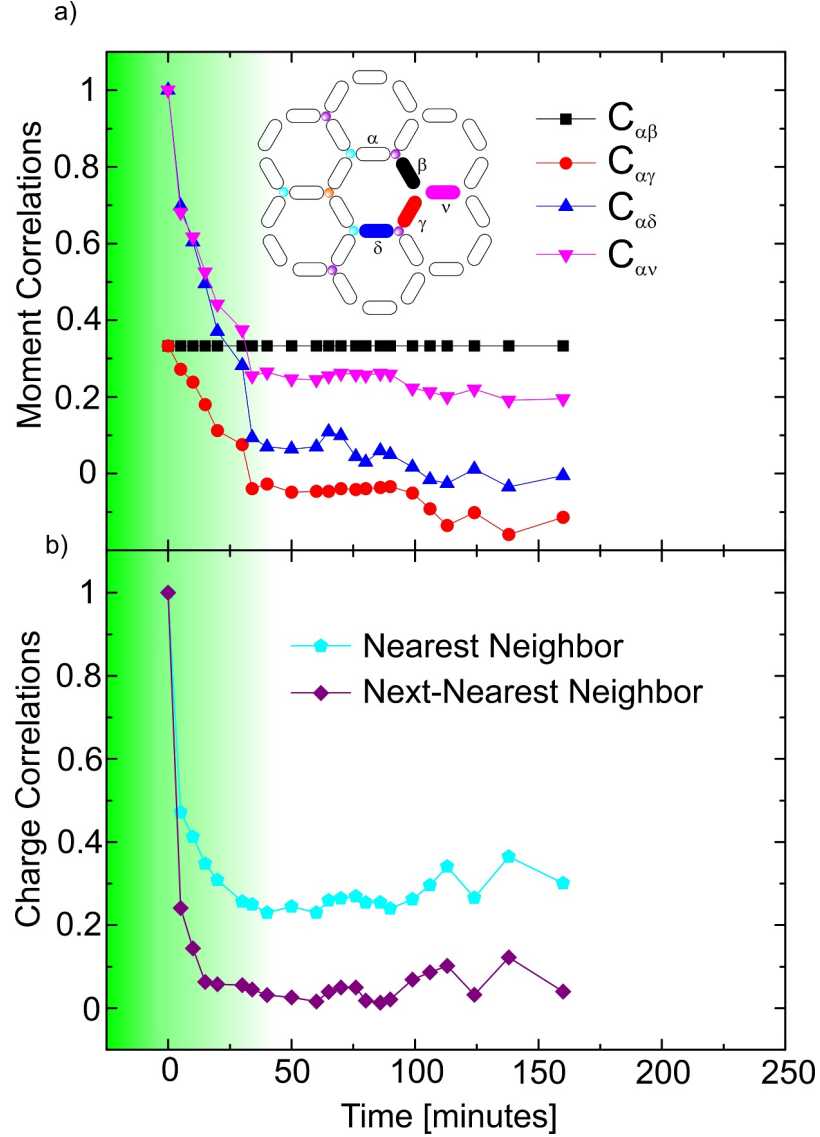


Figure 5.4: (a) Inter-nanomagnet moment correlation values and (b) charge-charge correlations, plotted as a function of time. The inset in (a) shows the kagome spin ice honeycomb structure, where each nanomagnet represents a single spin magnetic moment oriented along the nanomagnet's axis. The greek symbols label spins for correlation calculations.

structures, but due to limitations of the spatial resolution with PEEM both at the SLS and ALS, structures with nanomagnet dimensions of $L = 60 - 90$ nm and $W = 20 - 40$ nm could not be imaged in a satisfactory quality.

5.3.1 Continuous and Stepped Cooling

The sophisticated heating/cooling setup of PEEM3 at the ALS (see section 2.2.4) allowed us to explore a wider temperature range ($T = 40 - 390$ K) and investigate possibilities to achieve ground state configurations in artificial kagome spin ice, which was not possible with the annealing procedure applied in chapter 4.

As mentioned above, artificial kagome spin ice is predicted to undergo phase transitions from a superparamagnetic fully disordered state, down to an ordered, low-entropy configuration with ordered magnetic moments. Focusing on artificial kagome arrays with a blocking temperature of 160 K ($L = 300$ nm, $W = 100$ nm and $d = 2.5$ nm), we performed, as an initial step, two kinds of heating/cooling experiments, namely continuous and stepped cooling procedures [see Fig. 5.5 left panel]. Despite numerous repetitions of both heating/cooling procedures, no ground state configurations were observed [see Fig. 5.5 right panel], which supports the conclusion from chapter 4, that the predicted ground state is unlikely to be achieved in an infinite array of artificial kagome spin ice, at least with such simple heating/cooling procedures. Again, it might be that the blocking temperature of 160 K is still above the transition temperature to an ordered state [51].

5.3.2 Cycling around the blocking point

The results discussed so far suggest that more sophisticated annealing procedures are needed, in order to achieve ground state configurations in artificial kagome spin ice. The quest for such an annealing procedure raises parallels to an old optimization problem based on the so-called *simulated annealing* algorithm [67]. Simulated annealing is a probabilistic method that was proposed for finding global minima of *cost functions* that possess multiple local minima. The algorithm works by mimicking physical processes occurring while the system is slowly cooled down by a defined cooling schedule, allowing the system to finally freeze into a minimal energy configuration. Simulated annealing found its way to applications in various fields ranging from general optimization [67] to customized donor-matching models in heart transplantation [68].

Artificial kagome spin ice is highly frustrated and so far, we were not able to move beyond the highly disordered spin ice (K1) phase and the charge-ordered (K2) phase, which makes this system an ideal study case, in order to explore a heating/cooling protocol that allows the system in thermal equilibrium still to fall into ground state configurations. From all experiments performed so far, it became obvious that the dwell time of the system in lowest energy configuration is expected to be quite short, a fact that makes it very hard to observe any ground state configurations with our previously applied annealing protocols.

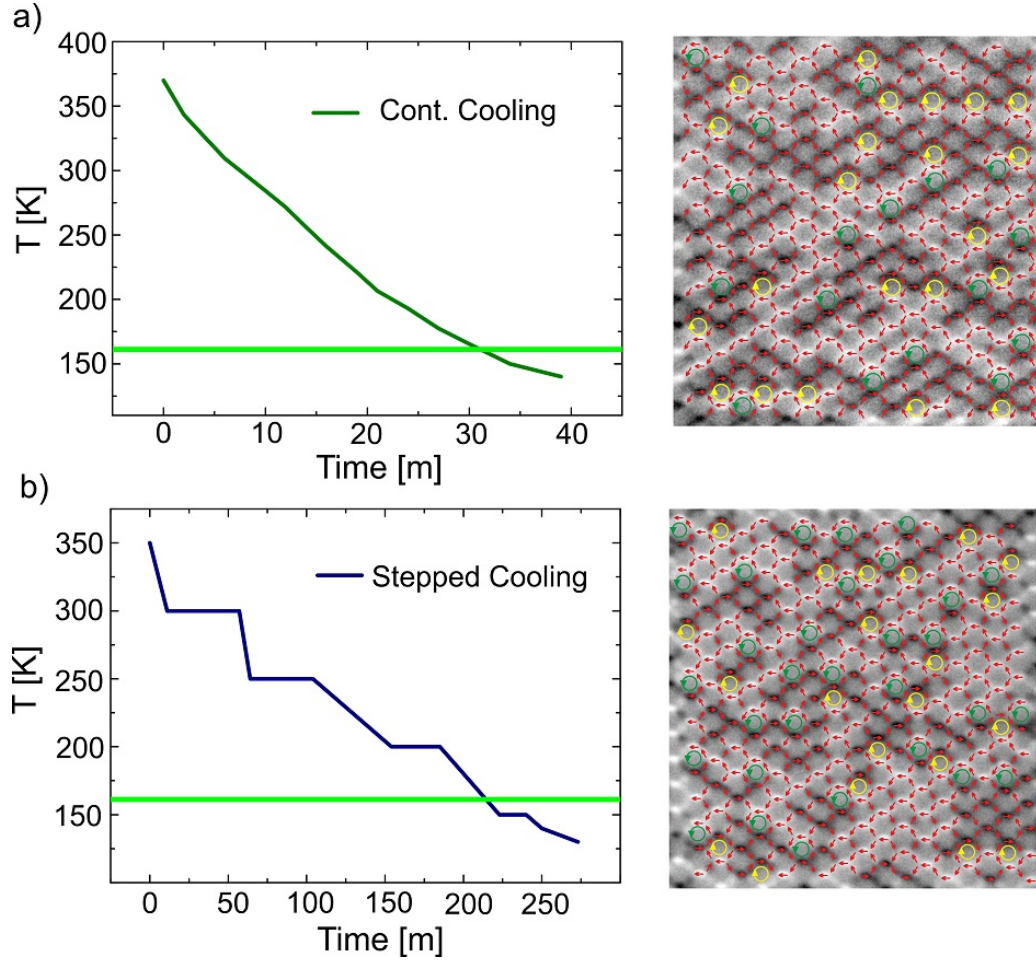


Figure 5.5: (a) Continuous cooling procedure: After heating the sample up to 370 K, it is cooled down below the blocking point (160 K) continuously within 35-40 minutes. Right panel: Below the blocking point, frozen-in configurations are XMCD imaged, revealing that, while several rings are in the vortex state, no ground state configurations were achieved. (b) Stepped cooling procedure: After heating the sample up to 350 K, it is cooled down below the blocking point (160 K) in a stepped manner, with several breaks, aimed to give the system more time to fall into its ground state configuration. Similar to the continuous cooling procedure, no ground state was observed (right panel). The yellow and green circles and arrows indicate clockwise and anti-clockwise vortices, respectively.

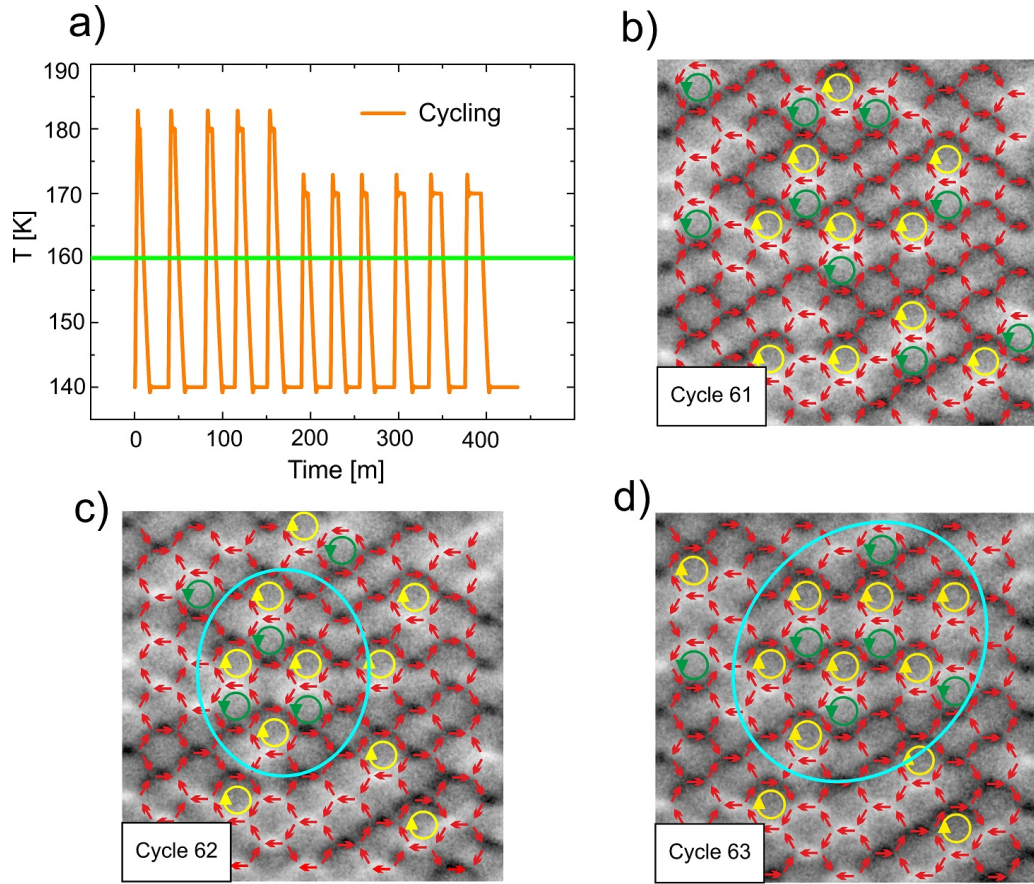


Figure 5.6: (a) Temperature cycling procedure, involving heating cooling around the blocking point. (b)-(d) XMCD images of artificial kagome spin ice recorded after temperature cycling of 61, 62 and 63 times, respectively.

This motivated us to implement a procedure that involves heating and cooling the system just slightly (5-20 K) above and below the blocking point ($T = 160K$) [see Fig. 5.6a], thus allowing *slow* dynamics within the system and capture configurational changes after cooling down. The idea is to allow a system in thermal equilibrium to briefly explore its phase space, eventually falling into local minimum configurations and freeze those configurations in. We periodically heated the sytem up to 170 K or 180 K, stayed 5-6 minutes at this temperature and cooled back down below the blocking point. Overall, we performed 64 temperature cycles of this kind, and observed local ground state configurations after each cycle. These ground state patches appeared and disappeared in different regions of the imaged array. The most successful case of emerging ground state domains was found in cycles Nr. 61-63, where a larger ground state domain consisting of up to 11 rings started

to grow between the cycles [see Fig. 5.6b-d]. Nonetheless, during the next cycle 64, the domain shrunk again, and at cycle 65 only one ground state unit cell remained.

Looking at the inter-nanomagnet moment and charge-charge correlations [see Fig. 5.7], one might conclude that the dynamics observed are indeed occurring within thermal equilibrium. Slight rises in the charge-charge correlation values with cycle number, are a direct indication of the emergence of ground state domains in these cycles. Simulations that will be performed by Peter Derlet (PSI) will deliver a direct comparison, allowing us to eventually conclude whether the observed ground state domains are a stochastic observation or a direct result of temperature cycling.

5.4 Conclusions

As mentioned in the introduction, the interpretation of the results presented in this chapter can be seen as preliminary, but one of the main conclusions that can already be made is that the predicted ground state configuration for artificial kagome spin ice is unlikely to be achieved with the procedure of saturating and heating, as presented in chapter 4. Instead, we observe how an initially ordered configuration (out-of-equilibrium state) rapidly moves towards thermal equilibrium into a disordered spin ice (K1) configuration. In addition, continuous and stepped cooling protocols from high temperatures of 370-390 K down to temperatures of 140 K are also not effective in terms of achieving ground state configurations.

With our proposed cycling procedure of moderate heating and cooling around the blocking point of an artificial kagome spin ice system, we were able to capture the system falling into local ground state configurations. While this method still does not represent a tool to achieve ground state configurations globally, it has enabled first ever observations of extended ground state domains in artificial kagome spin ice [see Fig. 5.6b-d].

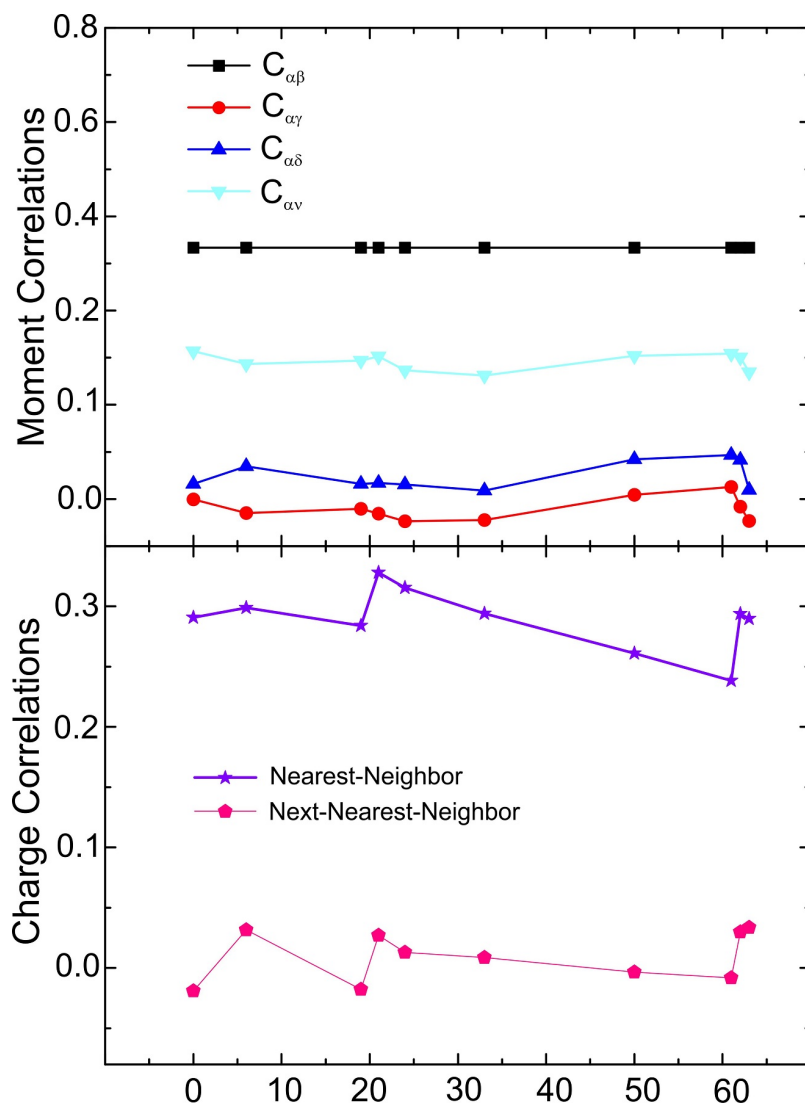


Figure 5.7: Inter-Nanomagnet moment correlations (upper graph) and charge-charge correlations (lower graph) as function of temperature cycles. Cycle Nr. 0 stands for the configuration achieved after cooling down from 370 K down to 140 K (blocking point $T = 160K$).

Chapter 6

Summary and outlook

The main goal of this project was to achieve artificial spin ice structures, comprising nanomagnets with thermally activated moment re-orientations. We were able to achieve this goal with a patterned Permalloy wedge film, which provides the advantage that the energy barriers for thermally driven moment fluctuations are varied in a controlled manner. At room temperature, depending on patterned nanomagnet dimensions (aspect ratio and height), we are able to move from frozen artificial spin ice configurations with no thermally induced moment fluctuations at higher film thicknesses, down to systems with fluctuating moments at lower film thicknesses (see chapter 4). We have investigated artificial spin ice structures both in the square (see chapter 3) and the kagome lattice geometry (chapter 4 and 5) with photoemission electron microscopy (PEEM) employing x-ray magnetic circular dichroism (XMCD) at the Fe L_3 edge. The combination of a patterned permalloy wedge film and XMCD imaging allowed us to directly observe and investigate thermally driven magnetic relaxation processes occurring in artificial spin ice systems (chapter 4-6).

6.1 Artificial Square Ice

In artificial square ice, we were able to directly observe thermal relaxation, going from an energetically excited state down to one of the two degenerate ground states. The relaxation process was found to go through two distinct regimes, namely a domain regime and a string regime. As soon as the system falls into a single ground state domain consisting only of Type I vertices, no further configurational changes are observed. This is an example of the confining potential associated with the Type III vertices occurring in two dimensional artificial square ice systems that dominates over the negligible Coulomb interaction between charged vertex pairs [25, 42, 50]. Experimental observations proved to be in good agreement with Kinetic Monte Carlo simulations based on a dipolar model, where each nanomagnet is replaced by a single dipole. Varying the interaction range from first nearest neighbor up to the sixth nearest neighbor, we were able to show that for artificial square ice considering

only nearest neighbor interactions is sufficient to achieve long-range ordered ground state configurations [25]. Our results proved the efficiency of thermal annealing in order to access long-range ordered ground state configurations in artificial square ice, in contrast to field-driven demagnetization protocols involving rotating samples in a decreasing magnetic field [6, 11]. Despite the ability to access the long range ordered ground state configurations in as-grown samples [8] or heating and cooling artificial square ice above and below the patterned material's Curie temperature [44, 45], our method is the only one that provides the ability to directly observe relaxation processes in real space and time. In addition to that, our direct comparison of the temporal evolution of the system in experimental observations and Kinetic Monte Carlo Simulations, delivered a direct evidence of the role of disorder (distribution of nanomagnet switching fields) on the temporal evolution of the investigated artificial square ice system [25].

So far, we were able to directly observe a full ground state ordering in extended arrays of artificial square ice and interestingly, as soon the systems fall into a 100% ground state configuration, no further dynamics are observed, which is explained by the strong confinement potential of artificial square ice in its ground state configuration. This can be understood by looking at the interaction energy as a function of Type III vertex separation length within a given background, in this case a Type I (ground state) background [see Fig. 3.5 blue circles and dotted line]. The creation of a pair of Type III vertex defects out of a Type I vertex background requires a significant amount of thermal energy. The energy Barrier, E , in Eqn. 4.2 will then be roughly around $(E_0 + \Delta E/2) = 1.5$ eV, thus, any excitations created within the ground state background will have a short life time, of the order of a few hundred milliseconds, thus much faster than the time scale of usual XMCD imaging. Towards the end of the PhD project, we performed some preliminary PEEM measurements using a single-polarization imaging mode (see experimental methods). This would theoretically allow us to observe configurational changes at a time scale of 500-700 ms, but issues with the image quality [see Fig. 3.6] over a large field of view at such short illumination times sustained and meant that a reliable analysis was not possible to be made. Scattering techniques, which just recently emerged [43], might allow the dynamics of artificial spin ice to be investigated at much shorter time scales.

Another interesting aspect of future investigations on artificial square ice is that recent numerical micromagnetic simulations clearly suggest distinct spectral features associated with the presence of vertex defects, which change in a systematic way for different string length connecting these defects [69]. These findings, which are so far based on micromagnetic simulations, will attract the interest of multiple experimental groups to investigate magnonics in artificial spin ice structures, both in the kagome and square ice geometry.

6.2 Artificial kagome spin ice

Regarding artificial kagome spin ice, which is highly frustrated and expected to be more complicated in behavior than artificial square ice, we used a more careful bottom-up approach focusing first on the so-called building block structures of artificial kagome spin ice, starting from one-ring structures up to seven-ring structures (see chapter 4). Using a simple thermal annealing procedure of saturating with an applied magnetic field and heating above the patterned nanomagnets' blocking temperature, we found out that this thermal annealing procedure is much more effective in achieving low-energy states in these building block structures, compared to demagnetization protocols, which involve rotating the sample in a decreasing magnetic field [10]. While we demonstrated this effectiveness to achieve low-energy states, we discovered an increasing difficulty to access the ground state configurations with increasing system size and, already at seven-ring structures, we were never able to observe the predicted ground state, despite multiple repetitions on over 40 seven rings. We were able to explain this by looking at the energy spectrum, which when multiplied by the Boltzmann factor [see Fig. 4.7], gives the density of states, showing that in order to access the ground states, annealing procedure have to be operated at much lower temperatures. In other words, the blocking temperature of the patterned nanomagnets needs to be below the predicted temperatures for phase transitions [52, 55]. Repeating this annealing procedure on extended arrays of artificial kagome spin ice, we confirm that the predicted ground state can not be accessed at all, using this simple annealing procedure. In comparison with previously observed field-driven motion of emergent magnetic monopoles in artificial kagome spin ice [12, 13, 70], we investigated the thermally driven behavior of emergent magnetic monopoles, which seem to be rather constrained and strongly dominated by strict obedience to the local ice-rule, which is obeyed in all experiments performed, so far (see chapter 5). Inter-nanomagnet moment correlations and the vertex charge-charge correlations show a drop from their maximum values (saturated state) to constant values at thermal equilibrium. The values at thermal equilibrium are in good agreement with previously reported correlations in frozen-in configurations of artificial kagome spin ice, following a similar annealing procedure of saturating, heating above the Curie point and cooling back to room temperature [45].

As a final quest towards the end of this PhD project, we tried to explore different methods and annealing protocols that would be more effective in achieving ground state configurations in artificial kagome spin ice. One of them was to move towards smaller nanomagnets ($300 \times 100 \text{ nm}^2$ surface instead of $470 \times 170 \text{ nm}^2$ and 2.5-3 nm height) with lower blocking temperatures for thermally activated moment reorientations ($T_B = 160\text{K}$). Procedures involving a *continuous cooling* and *stepped cooling* from 370-390 K, down to 140 K did not result to observations of any ground state configurations (see Chapter 5), despite numerous repetitions. The system is found to be captured in a spin ice II phase (K2), with charge-ordered regions and multiple clockwise and anti-clockwise vortices being observed.

Inspired by an old optimization algorithm, generally known as *simulated annealing* [67], we pursued a temperature protocol that involved repeated heating and cooling, just slightly above and below the blocking point, with short dwell times at the peak temperature, so that advantageous configurational changes are captured and frozen in after cooling down below the blocking point. While this method still does not represent a procedure to obtain a global ground state, it is the only method, so far, that allows us to grow larger patches falling into the predicted ground state configuration (see chapter 5). Future investigations on optimized annealing protocols might involve the combination of thermal annealing and the application of AC fields, all possibly applied at the same time.

Bibliography

- [1] M. F. Shlesinger, and E. W. Montroll, Proceedings of the National Academy of Sciences of the United States of America-Physical Sciences **81**, 1280 (1984).
- [2] R. G. Palmer, D. L. Stein, E. Abrahams, P. W. Anderson, Physical Review Letters **53**, 958 (1984).
- [3] M. Levantino, A. Cupane, L. Zimanyi, and P. Ormos, Proceedings of the National Academy of Sciences of the United States of America **101**, 14402 (2004).
- [4] Y. Han, Y. Shokef, A. M. Alsayed, P. Yunker, T. C. Lubensky and A. G. Yodh, Nature **456**, 898 (2008).
- [5] A. Farhan, P. M. Derlet, A. Kleibert, A. Balan, R.V. Chopdekar, M. Wyss, L. Anghinolfi, F. Nolting, L.J. Heyderman, Nature Physics **9**, 375 (2013)
- [6] R. F. Wang, C. Nisoli, R. S. Freitas, J. Li, W. McConville, B. J. Cooley, M. S. Lund, N. Samarth, C. Leighton, V. H. Crespi, and P. Schiffer, Nature **439**, 303 (2006).
- [7] M. J. Harris, S. T. Bramwell, D. F. McMorrow, T. Zeiske, and K. W. Godfrey, Physical Review Letters **79**, 2554 (1997).
- [8] J. P. Morgan, A. Stein, S. Langridge, and C. H. Marrows, Nature Physics **7**, 75 (2011).
- [9] Y. Qi, T. Brintlinger, and J. Cumings, Physical Review B **77**, 094418 (2008).
- [10] E. Mengotti, L. J. Heyderman, A. Fraàle-Rodriguez, A. Bisig, L. Le Guyader, F. Nolting, and H. B. Braun, Physical Review B **78**, 144402 (2008).
- [11] M. Tanaka, E. Saitoh, H. Miyajima, T. Yamaoka, and Y. Iye, Physical Review B **73**, 052411 (2006).
- [12] S. Ladak, D. E. Read, G. K. Perkins, L. F. Cohen and W. R. Branford, Nature Physics **6**, 359 (2010).
- [13] E. Mengotti, L. J. Heyderman, A. Fraàle-Rodriguez, F. Nolting, R. V. Hügli, and H. B. Braun, Nature Physics **7**, 68 (2011).

- [14] W. Kinzel, and K. H. Fischer, *Solid State Communications* **23**, 687 (1977).
- [15] J. Snyder, J. S. Slusky, R. J. Cava and P. Schiffer, *Nature* **413**, 48 (2001).
- [16] G. J. Nieuwenhuys and J. A. Mydosh, *Physica B & C* **86** 880 (1977).
- [17] Z. D. Chen, *Physical Review B* **53**, 6499 (1996).
- [18] G. Toulouse, S. Dehaene, and J. P. Changeux, *Proceedings of the National Academy of Sciences of the United States of America* **83**, 1695 (1986).
- [19] J. D. Bryngelson, and P. G. Wolynes, *Proceedings of the National Academy of Sciences of the United States of America* **84**, 7524 (1987).
- [20] N. Surlas, *Nature* **339**, 693 (1989).
- [21] S. T. Bramwell, M. J. P. Gingras, *Science* **294**, 1495 (2001).
- [22] W. F. Giauque, M. F. Ashley, *Physical Review*. **43**, 81 (1993).
- [23] L. Pauling, *Journal of the American Chemical Society* **57** 2680 (1935).
- [24] D. Bernal, R. H. Fowler, *Journal of Chemical Physics* **1**, 515 (1933).
- [25] A. Farhan, P. M. Derlet, A. Kleibert, A. Balan, R. V. Chopdekar, M. Wyss, J. Perron, A. Scholl, F. Nolting, and L. J. Heyderman, *Physical Review Letters* **111**, 057204 (2013).
- [26] A. S. Wills, R. Ballou, and C. Lacroix, *Physical Review B* **66** 144407 (2002).
- [27] Y. Tabata, H. Kadowaki, K. Matsuhira, Z. Hiroi, N. Aso, E. Ressouche, and B. Fåk, *Physical Review Letters* **97**, 257205 (2006).
- [28] L. Le Guyader, A. Kleibert, A. F. Rodriguez, S. El Moussaoui, A. Balan, M. Buzzi, J. Raabe, and F. Nolting, *Journal of Electron Spectroscopy and Related Phenomena* **185**, 371 (2012).
- [29] J. Stöhr, Y. Wu, B. D. Hermsmeier, M. G. Samant, G. R. Harp, S. Koranda, D. Dunham, and B. P. Tonner, *Science* **259**, 658 (1993).
- [30] N. Rougemaille, F. Montaigne, B. Canals, A. Duluard, D. Lacour, M. Hehn, R. Belkhou, O. Fruchart, S. El Moussaoui, A. Bendounan, and F. Maccherozzi, *Physical Review Letters* **106**, 057209 (2011).
- [31] U. Flechsig, F. Nolting, A. Fraile-Rodriguez, J. Krempasky, C. Quitmann, T. Schmidt, S. Spielmann, and D. Zimoch, *AIP Conf. Proc.* **1234**, 319 (2010).
- [32] C. Quitmann, U. Flechsig, L. Patthey, T. Schmidt, G. Ingold, M. Howells, M. Janousch, and R. Abela, *Surface Science* **480**, Nr. 3, 173 (2001).

- [33] J. Stöhr, *NEXAFS Spectroscopy*, vol. 25. Heidelberg, Germany: Springer Series in Surface Sciences (1992).
- [34] E. Beaupaire, H. Bulou, F. Scheurer, and J. Kappler, *Magnetism and synchrotron radiation*, vol. 133. Berlin Heidelberg: Springer Proceedings in Physics (2010).
- [35] F. Nolting, *Magnetic Imaging with X-rays*, vol. 133. Berlin Heidelberg: Springer-Verlag, 2010. Chapter 12, pp. 345- 366.
- [36] A. Doran, M. Church, T. Miller, G. Morrison, A. T. Young, and A. Scholl, *Journal of Electron Spectroscopy and Related Phenomena* **185**, 340 (2012).
- [37] G. Möller and R. Moessner, *Physical Review Letters* **96**, 237202 (2006).
- [38] Z. Budrikis, K. L. Livesey, J. P. Morgan, J. Akerman, A. Stein, S. Langridge, C. H. Marrows and R. L. Stamps, *New Journal of Physics* **14**, 035014 (2012).
- [39] W. M. Young and E. W. Elcock, *P. Phys. Soc. Lond* **89**, 735 (1966).
- [40] S. Krause, G. Herzog, T. Stapelfeldt, L. Berbil-Bautista, M. Bode, E.Y. Vedmedenko, and R. Wiesendanger, *Physical Review Letters*, **103**, 127202 (2011).
- [41] Z. Budrikis, P. Politi, and R. L. Stamps, *Physical Review Letters* **107**, 217204 (2011).
- [42] L. A. Mól, R. L. Silva, R. C. Silva, A. R. Pereira, W. A. Moura-Melo and B. V. Costa, *J. Appl. Phys.* **106**, 063913 (2009).
- [43] J. Perron, L. Anghinolfi, B. Tudu, N. Jaouen, J.-M. Tonnerre, M. Sacchi, F. Nolting, J. Lüning, and L. J. Heyderman, *Physical Review B* **88**, 214424 (2013).
- [44] J. M. Porro, A. Bedoya-Pinto, A. Berger and P. Vavassori, *New Journal of Physics* **15**, 055012 (2013).
- [45] S. Zhang, I. Gilbert, C. Nisoli, G.W. Chern M. J. Erickson, L. O'Brien, C. Leighton, P. E. Lammert, V. H. Crespi, and Peter Schiffer, *Nature* **500**, 553 (2013).
- [46] M. Pärnaste, M. Marcellini, Erik Holmström, N. Bock, J. Fransson, O. Eriksson and B. Hjörvarsson, *J. Phys.: Condens. Matter* **19**, 246213 (2007).
- [47] E. Th. Papaioannou, V. Kapaklis, A. Taroni, M. Marcellini and B. Hjörvarsson, *J. Phys.: Condens. Matter* **22**, 236004 (2010).
- [48] V. Kapaklis, U. B. Arnalds, A. Harman-Clarke, E. Th. Papaioannou, M. Karimipour, P. Korelis, A. Taroni, P. C. W. Holdsworth, S. T. Bramwell and B. Hjörvarsson, *New Journal of Physics*, **14**, 035009 (2012).

- [49] U. B. Arnalds, A. Farhan, R. V. Chopdekar, V. Kapaklis, A. Balan, E. Th. Papaioannou, M. Ahlberg, F. Nolting, L. J. Heyderman and B. Hjörvarsson, *Applied Physics Letters* **101**, 112404 (2012).
- [50] R. C. Silva, F. S. Nascimento, L. A. S. Mol, W. A. Moura-Melo, and A. R. Pereira, *New Journal of Physics* **14**, 015008 (2012).
- [51] A. Farhan, A. Kleibert, P. Derlet, L. Anghinolfi, A. Balan, R. V. Chopdekar, M. Wyss, S. Gliga, F. Nolting, L. J. Heyderman, *Physical Review B* **89**, 214405 (2014).
- [52] G. Moller and R. Moessner, *Physical Review B* **80**, 140409(R) (2009).
- [53] J. Rothman, M. Kläui, L. Lopez-Diaz, C. A. F. Vaz, A. Bleloch, J. A. C. Bland, Z. Cui, and R. Speaks, *Physical Review Letters* **86**, 1098 (2001).
- [54] R. V. Chopdekar, G. Duff, R. V. Hügli, E. Mengotti, D. A. Zanin, L. J. Heyderman, and H. B. Braun, *New Journal of Physics* **15**, 125033 (2013).
- [55] G. W. Chern, P. Mellado, and O. Tchernyshyov, *Physical Review Letters* **106**, 207202 (2011).
- [56] D. Levis, L. F. Cugliandolo, L. Foini, and M. Tarzia, *Physical Review Letters* **110**, 207206 (2013).
- [57] S. T. Bramwell, S. R. Giblin, S. Calder, R. Aldus, D. Prabhakaran, and T. Fennell, *Nature* **461**, 956 (2009).
- [58] D. J. P. Morris, D. A. Tennant, S. A. Grigera, B. Klemke, C. Castelnovo, R. Moessner, C. Czternasty, M. Meissner, K. C. Rule, J.-U. Hoffmann, K. Kiefer, S. Gerischer, D. Slobinsky, R. S. Perry, *Science* **326**, 411 (2009).
- [59] L. D. C. Jaubert, and P. C. W. Holdsworth, *Nature Physics* **5**, 258 (2009).
- [60] A. Farhan et al., in preparation.
- [61] A. Farhan et al., in preparation.
- [62] P. A. M. Dirac, *Proceedings of the Royal Society London A* **133**, 60 (1931).
- [63] K. A. Milton, *Reports on Progress in Physics*, **69**, 1637 (2006).
- [64] C. Castelnovo, R. Moessner, and S. L. Sondhi, *Nature* **451**, 42 (2008).
- [65] A. P. Ramirez, A. Hayashi, R. J. Cava, R. Siddharthan, and B. S. Shastry, *Nature* **399**, 333 (1999).

- [66] L. Bovo, J. A. Bloxsom, D. Prabhakaran, G. Aeppli, and S. T. Bramwell, *Nature Communications* **4**, 1535 (2012).
- [67] S. Kirkpatrick, C. D. Gelatt Jr., and M. P. Vecchi, *Science* **220**, 671 (1983).
- [68] D. Ansari, B. Andersson, M. Ohlsson, P. Höglund, R. Andersson, and J. Nilsson, *Scientific Reports* **3**, 1922 (2013).
- [69] S. Gliga, A. Kakay, R. Hertel, and O. G. Heinonen, *Physical Review Letters* **110**, 117205 (2013).
- [70] R. V. Hügli, G. Duff, B. O’Conchuir, E. Mengotti, A. Fraàle-Rodriguez, F. Nolting, L. J. Heyderman and H. B. Braun, *Phil. Trans. R. Soc. A*, **370**, 5767 (2012).

List of Publications

1. V. Kapaklis, U. B. Arnalds, **A. Farhan**, R. V. Chopdekar, A. Balan, A. Scholl, L. J. Heyderman, and B. Hjörvarsson, *Nature Nanotechnology* **9**, 514 (2014).
2. **A. Farhan**, A. Kleibert, P. Derlet, L. Anghinolfi, A. Balan, R. V. Chopdekar, M. Wyss, S. Gliga, F. Nolting, L. J. Heyderman, *Physical Review B*, **89**, 214405 (2014).
3. **A. Farhan**, P. M. Derlet, A. Kleibert, A. Balan, R.V. Chopdekar, M. Wyss, L. Anghinolfi, F. Nolting, L.J. Heyderman, *Nature Physics* **9**, 375 (2013).
4. **A. Farhan**, P. M. Derlet, A. Kleibert, A. Balan, R. V. Chopdekar, M. Wyss, J. Perron, A. Scholl, F. Nolting, and L. J. Heyderman, *Physical Review Letters* **111**, 057204 (2013).
5. U. B. Arnalds, **A. Farhan**, R. V. Chopdekar, V. Kapaklis, A. Balan, E. Th. Papaioannou, M. Ahlberg, F. Nolting, L. J. Heyderman and B. Hjörvarsson, *Applied Physics Letters* **101**, 112404 (2012).
6. L. Wang, B. Terhalle, V. A. Guzenko, **A. Farhan**, M. Hojeij and Y. Ekinici, *Applied Physics Letters* **101**, 093104 (2012).
7. J. Heidler, J. Rhensius, C. A. F. Vaz, P. Wohlhüter, H. S. Körner, A. Bisig, S. Schweitzer, **A. Farhan**, L. Méchin, L. Le Guyader, F. Nolting, A. Locatelli, T. O. Montes, M. A. Niño, F. Kronast, L. J. Heyderman and M. Kläui, *Journal of Applied Physics* **112** 103921 (2012).